Journal of Archaeological Science: Reports 49 (2023) 103914

Contents lists available at ScienceDirect

Journal of Archaeological Science: Reports

journal homepage: www.elsevier.com/locate/jasrep

Fire at the gate of Hazor: A micro-geoarchaeological study of the depositional history of a Bronze Age City gate

Marko Runjajić [a,*], Yosef Garfinkel [b], Michael G. Hasel [c], Assaf Yasur-Landau [a], David E. Friesem [a,d]

[a] Recanati Institute for Maritime Studies, Department of Maritime Civilizations, School of Archaeology and Maritime Cultures, University of Haifa, Israel
[b] Institute of Archaeology, The Hebrew University of Jerusalem, Israel
[c] Institute of Archaeology, Southern Adventist University, USA
[d] Haifa Center for Mediterranean History, University of Haifa, Israel

ARTICLE INFO

Keywords:
Tel Hazor
Late Bronze Age
Gate
Destruction
Micro-geoarchaeology
FTIR
Phytoliths

ABSTRACT

The City of Hazor is one of the most significant archaeological sites from the biblical period in Israel. Studies on destruction have received much attention in archaeology in recent years. Previous excavations in Hazor have suggested a major conflagration event that destroyed the entire tell site at the end of the Late Bronze Age. The present study re-examines the sedimentary sequence of one of the city's gates located in Area K by applying a suite of micro-geoarchaeological analyses to understand the stratigraphy previously documented by Yigael Yadin (1972) and later also interpreted by Amnon Ben-Tor et al. (1989); Ben-Tor (1993, 2016); Bechar et al. (2021). In the summer of 2019, 89 bulk sediment samples were taken within squares K5 and K7 in the gate's passage. This study aimed to understand the archaeological formation processes at the gate and interpret human activities in the Lower City gate of Hazor based on the micro-archaeological record. Laboratory work included Fourier-transform infrared (FTIR) spectroscopy to analyze sediment samples' composition and quantify phytoliths, wood ash, and dung spherulite concentrations. The major goals of this study are: a) to study the site formation processes, based on mineralogical assemblages and activity micro-residues, of a Middle Bronze to Late Bronze Age city gate; b) to identify mineralogical- and micro-remains, as indicators for fire and destruction of the gate; c) to identify occupation surfaces within the gate and their associated micro-residues; and d) to re-examine previous interpretations of the history of the gate and Hazor in light of the micro-archaeological record.

The results confirmed Yadin's interpretation of the occupation levels at stratum 3 (MB II-C) and 2 (LB I), but with no evidence for destruction between the strata. Those strata showed typical tell site remains, such as anthropogenic input of ash and phytoliths, indicating more or less continuous urban activity. For Yadin's stratum 1B gate, we identified the floor, the roof, which was the main element that burnt, overlain by a thick unburnt accumulation of the second floor and final burnt debris atop. Our study also suggested a sequence of events for the fiery destruction of the gate and its collapse. The distribution of phytoliths and wood ash combined with the sediments' composition proposes a single collapse event caused by fire from within the gate. The minimal anthropogenic record above the destruction horizon indicates possible disuse of the gate area following this major destruction event. The conclusions of this study offer new and direct evidence for the history of the gate at Hazor's Lower City with continuous activity from the Middle Bronze into the Late Bronze Age, ending with a major and single event of destruction of the site at the end of the Late Bronze Age which was followed by its abandonment.

1. Introduction

Tell Hazor, situated in the north of modern Israel, is the largest archaeological site in the southern Levant, with an area of 84 ha (Fig. 1a). The tell site, excavated in the mid-1950s and 60s (Fig. 1b), with ongoing excavation to this day, once stood at the center of a powerful regional polity that dominated northern Canaan from the Middle Bronze Age II (ca. 1750 BCE) to its destruction during the 13th

* Corresponding author.
E-mail address: marko@mailbox.org (M. Runjajić).

https://doi.org/10.1016/j.jasrep.2023.103914
Received 1 September 2022; Received in revised form 15 February 2023; Accepted 21 February 2023
Available online 21 March 2023
2352-409X/

century BCE (Late Bronze Age IIB) (Yadin, 1972; Ben-Tor, 1993; 2016). The collapse of the largest urban center at Canaan occurred during the troubled years of the Late Bronze Age, a period of the widespread collapse of societies in the eastern Mediterranean (e.g., Cline, 2014; Knapp and Manning, 2016). This destruction was attributed by the excavators Yadin and Ben-Tor to a violent conquest by the Israelites, accompanied by a conflagration dated to ca. 1230 BCE (Yadin, 1972: 108; Ben-Tor, 1993: 599; Ben-Tor, 2016: 117). However, Zuckerman (2007, 2011) suggested an internal revolt following a period of civil unrest. The destruction of the Upper City is well documented in recent studies on the burning of the ceremonial palace and its environs (Ben-Tor et al., 2017; Kreimerman, 2017).

Yadin's excavations in the vast Lower City of Hazor (see Table 1 for Lower City stratigraphy; Fig. 1b-c) have argued for multiple destruction events during the Late Bronze Age. The first, by Thutmose III during the Late Bronze Age I, is represented by the end of stratum 3. Later destruction is ascribed to the Egyptian Pharaoh Seti I at the beginning of the 13th century BCE, visible in stratum 1B (Yadin, 1959; 1972: 108). The final destruction in the last occupation phase of the Lower City is ascribed to stratum 1A being associated with the Israelites (Yadin, 1972: 108-109; Ben-Tor, 1993: 603). After that, the Lower City ceases to exist, while the archaeological remains within the Upper City show almost continuous activities up to Hellenistic times (e.g., Yadin, 1972).

One of the keys to understanding the turbulent settlement history of the Lower City is the massive gate complex in Area K in the Lower City (Fig. 1b). While a second gate complex of similar dimensions was found in Area P (Fig. 1b), most of its cardinal remains were destroyed by road construction works during the 1920s (Yadin, 1969: 59-61; Yadin, 1972: 63-65; Ben-Tor et al., 1997: 353–389). Placing focus on the Area K gate complex, it was first constructed during MB II with a revetment wall built in cyclopean masonry. Changes in the plan of the gate continued until the LB II-B period. Within the gate, Yadin argued for two destruction events, the first during the end of stratum 3 in LB I, the other at the end of stratum 1A during LB II, which included a deposit 1.5 m thick described as collapsed burnt mud bricks (Yadin, 1972: 59-73, 108-109; Ben-Tor et al., 1989: 292-293). The excavators of the area for the Yadin expedition, Dothan and Dunayevsky, and later Finkelstein, who reassessed the documentation given by Yadin, attributed the destruction layer to stratum 1B (Ben-Tor et al., 1989: 297; Finkelstein, 2005: 344–345). In general, Ben-Tor recognized two destruction layers for the entire city, corresponding to both stratum 1B and stratum 1A (Ben-Tor and Zuckerman, 2008: 2, 5: Table 1), whereas his attribution of the gate's destruction in Area K has shifted between the strata 1A and 1B (Ben-Tor et al., 1989; Ben-Tor, 1993, 2016).

Most recently, according to Ben-Tor's understanding, though the prior occurring decline for the city is recognized, all of Hazor was destroyed within the last LB stratum (1A in the Lower City) in a fierce conflagration (Bechar et al., 2021: 69). Bechar and the co-authors, on the other hand, placed Hazor's demise at the end of 1B, arguing for a decline within 1A and secondary use of the monumental structures, such as temples. Beyond that, their modeling option generated a void of a yet undefined stratum for the LB II-A/ LB II-B period in the Lower City (Table 1; Bechar et al., 2021: 67–68).

In August 2019 (Fig. 1c), an expedition led by Yosef Garfinkel re-excavated parts of Area K to better understand the chrono-stratigraphic sequence of the gate complex in order to shed new light on the destruction, occupation- and abandonment episodes in Hazor's Lower City. The main objective of the 2019 campaign was to reassess the observations given by previous excavators involved in the debate.

In the 1989 publication, the stratigraphical sub-division of 1B in Area K within the LB II is notable (Ben-Tor et al., 1989: 297). In 1967, within the scarce remains of the other gate in Area P, several successive floor levels were recognized for the LB II phases (Ben-Tor et al., 1997: 353–368). Over and above these sub-strata, the recent radiocarbon study by Bechar et al. (2021) suggested a gap for the Lower City between strata 1B and 1A (Table 1; Bechar et al., 2021). Despite the field observations for Area K published in the volumes of 1961 and 1989, the gate's use and collapse have been an enigma for the scientific

Table 1
Showing Chronological overview for Hazor from the Middle Bronze Age until the Iron Age. Adapted from Bechar et al. (2021); and from Zuckerman (2012): "Chronological table of Canaanite Hazor (after Yadin, 1972, 118 and Ben-Tor, 1993, 606)." Bechar *et al.*'s version integrated radio carbon analysis (here Option A). For the LB II strata, samples from Area S (see Fig. 1) propose a span between 1A and 1B.

after Zuckerman (2012) Absolute Dates (B.C.E.)	Lower City	Upper City	Periods	Historical References
18th – 17th cents.	4	XVII	MB II-A-B	Mari Archive
17th – 16th cents.	3	XVI	MB II-C	
after Bechar et al. (2021)				
~1550–1457/6	**2**	XV	**LB I-A**	Annals of New Kingdom Pharaohs
~1457/6–1300	**1B**	XIV	**LB I-B - LB II-A**	Amarna Archive
~1300–1250		XIII	**LB II-A - LB II-B**	Papyrus Anastasi I
1250–1230/1200	**1A**		**LB II-B**	
11th cent.	——	XII-XI	IA I	

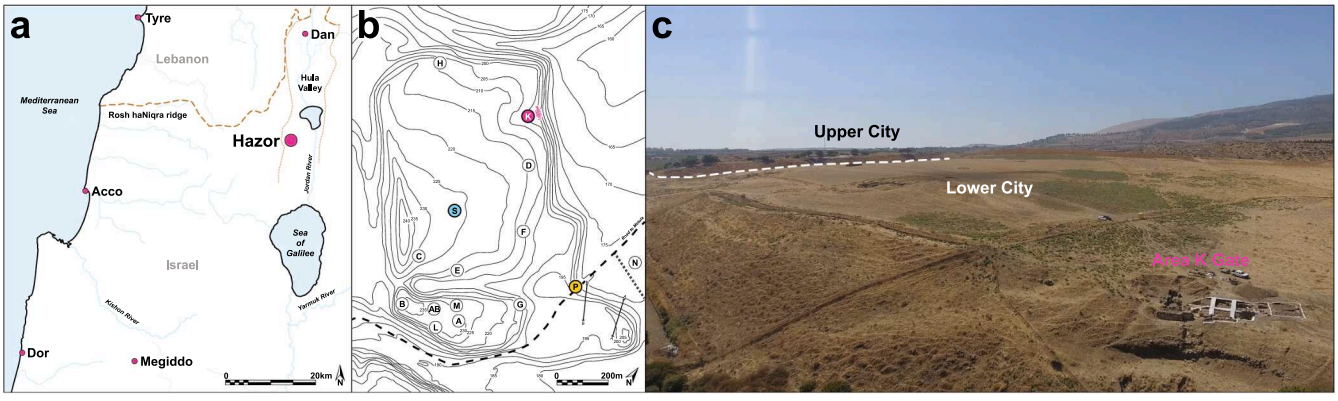

Fig. 1. Site maps. **(a)** Location of Hazor. **(b)** Site plan of the areas excavated by Yadin, Location of Area K gate complex marked in pink. Area P with the second Lower City gate highlighted in red (after Bechar et al., 2021: Fig. 1.; adapted). In blue Area S (excavated by Yadin in the form of a sounding A1/210 in 1957 and later beginning in 2008 as Area S within three seasons by Zuckerman). Sample location of radiocarbon analysis by Bechar et al., 2021 (dates seen in Table 1). In orange color location of the second gate in Area P. **(c)** Aerial view of Hazor in 2019 from the north. In the back, the tell with the Upper City, below the Lower City. At the north-western edge, Area K with its gate during our expedition. (photo: H. Nativ).

community.

As part of the expedition, a micro-archaeological study was conducted in the section of the gate which Yadin excavated. After cleaning, this section running through the gate's passageway provided the stratigraphic sequence from stratum 3 to 1. The study aimed to understand the sedimentary sequence of Area K, with a particular emphasis on identifying any destruction events. It used insights from micro-geoarchaeological studies conducted at tell sites in Israel, which provided new high-resolution understandings of archaeological formation processes and human activities during the Bronze and Iron Ages (Shahack-Gross et al., 2005, 2009; Albert et al., 2008). Specifically, micro-residues served in reconstructing exposures to fire events (Berna et al., 2007; Eliyahu-Behar et al., 2008; Namdar et al., 2011; Gur-Arieh et al., 2014; Forget et al., 2015; Regev et al., 2015; Kreimerman and Shahack-Gross, 2019; Kreimerman 2021), occupation layers and construction materials (Shahack-Gross et al., 2005; Albert et al., 2008, Shahack-Gross et al., 2009; Regev et al., 2015; Sapir et al., 2016).

2. Study Area (Area K, Hazor's Lower City)

In 1958, Yadin unearthed half of the gate in Area K, creating a section along the passageway axis (Fig. 2a). According to Yadin, the gate complex could be divided into five phases, designated strata 1A, 1B, 2, 3, and 4 (Yadin, 1972: 58). In 1989, Ben-Tor shifted the designation of 1A and 1B strata to "Post-1A" (unique designation for all of Hazor) and 1B-1A (Ben-Tor et al., 1989: 297). In 2019 our team unearthed seven squares in the gate area, including the central passage (Fig. 2b-c). The passage sequence was divided into squares K5 and K7 (Fig. 3a).

At the bottom of square K7 (Fig. 3a), Yadin's floor 5038 (Fig. 2a; Fig. 3b; Yadin et al., 1961: Pl. CXXXIII: 1) of stratum 3 is recognized with its stone slabs (Fig. 3b-c). Above it, loci L12067 and L12062 are considered to be fill deposits. A chalky plaster floor in-between these fills, L12065 determined as paving 5002 in 1958 (Fig. 3a, c; Yadin et al., 1961: Pl. CXXXIV: 1), was observed resting on top of Yadin's floor 5038, at 190.51–190.72 mamsl. Floor L12060 (Fig. 3c-d), made of a yellowish chalky impression, is at 190.72–191.12 masml and is attributed to Yadin's floor 5020 of locus 5020/1 (Ben-Tor et al., 1989: 285). The floor L12060 is 0.15 m thick and spreads over a 0.4 m thick layer (Fig. 3c-d). Above this floor (Fig. 3d), a fill (L12029) is characterized by dark compact soil and unhewn fieldstones. In the layer above it, L12016, smaller pebbles and small pieces of pottery are found. A thin plaster make-up L12045 caps the top of L12016. To the north of L12045, a chalky layer, L12050, was found directly beneath the topsoil, possibly a continuation of a plaster floor belonging to L12045. This part of the profile is poorly preserved; this layer cannot be interpreted for now. The soil of 0.05 m in thickness, L12015, separates this thin plaster layer (L12045) from the pebble floor L12040 above it (Fig. 3b; Yadin's floor 5004 of stratum 1B; Yadin, 1972: 62-63). The pebble floor (L12040) is at 191.73–191.79 mamsl.

In square K5 (Fig. 4), a profile (Fig. 4a) was established along the

Fig. 2. Area K gate complex. The first digit '1′ is omitted in the elevations provided on the plans by Ben-Tor et al. (1989). **(a)** Phase plan of the gate showing strata 4 to 1, with excavated soundings in 1958. (from Ben-Tor et al., 1989: Plan XLII) 2019 profiles of K5 (orange) and K7 (blue) marked in the plan. In pink, the cross-section (C^1-C^2) through the gate passage is displayed below the phase plan. Note that 5004 refers to 1B. (from Ben-Tor et al., 1989: Plan XLIV) Pebble floor 5004 is visible in the center of the cross-section. To the left (northern part of the gate), K7 marking the re-excavated area in 5020/1. Correlation to sounding 5020 for later strata. **(b)** Aerial, showing the seven squares of the 2019 excavation campaign. For this study, relevant profiles of squares K5 (orange) and K7 (blue) are marked. (c) Stone plan of 2019 expedition, with K5 and K7 profiles marked. In K5 and K7, 89 bulk sediments were taken (see section 3). (adapted; plan: E. Arkin-Shalev) **(c)** Stone plan of stratum 1B (Ben-Tor et al., 1989: Plan XLIII) showing the profiles of K5 and K7 established in 2019, in relation to pebble floor 5004. **(d)** Stone plan of stratum 1B (from Ben-Tor et al., 1989: Plan XLIII) shows the profiles of K5 and K7 established in 2019, concerning pebble floor 5004.

Fig. 3. Square K7 shows the loci distinguished during the 2019 expedition. **(a)** 2019 aerial view from the north on the gate passage with square K7 in front. K5 in the back. Loci of K7 are shown in Fig. 3c-d marked in the photo. **(b)** Showing the northern area of the gate passage, the entrance, with floor 5038 of stratum 3 during the 1958 excavation. (from Yadin et al., 1961: Pl. CXXXIV:1) Location of our K7 from 2019. **(c)** Bottom of section. The surface of the gate passage of Yadin's stratum 3 with stone blocks, 5038. Above are fills 12067 and 12062. Floor 12065, corresponding to Yadin's paving 5002 in-between. Teal double-arrow connecting the top and bottom of floor 12060 and its continuation in Fig. 3d. **(d)** Upper section. At the bottom floor L12060, corresponding to Yadin's sounding 5020, mentioning the level of stratum 2. Above fills L12029 and L12016, indicated with teal dotted lines. To the right chalky (floor) patches, plaster L12045, and chalky layer L12050. An additional fill is seen in L12015. Above it, pebble floor L12040 corresponds to Yadin's 5004. L12014 shows rubble or disturbed layer. (photo a: H. Nativ; photos c and d: E. Arkin-Shalev).

gate passage in elongation of the middle pier and divided into loci L12033 and L12034 (Fig. 2; Fig. 4a-b). This profile was indented compared to Yadin's cross-section (Fig. 2c-d; Fig. 4a-c). While the area was mainly composed of backfill, mud brick debris appeared upon indenting. Above the pebble floor L12018 at 191.79–191.93 mamsl, three layers roughly 11 cm thick were encountered (Fig. 4b): (1) L12032, a sediment fill; (2) L12031 described as a thin plaster make-up with an approximate thickness of 2 cm; and (3) a potential other floor, L12030, resting above the previous layers. The stones of this floor (L12030) are similar to Yadin's pebble floor 5004 (Fig. 2c-d; Fig. 4c). L12030 could be considered a later phase of the pebble floor L12018. That would correlate with the subdivision provided in 1989 (Ben-Tor et al., 1989: 297). Within the cleaned profile of K5, bulk sediments were sampled. Ashes (Fig. 4d) and mud bricks (Fig. 4, sample location 57) were visible in parts of the section.

3. Materials and methods

3.1. Materials

Bulk sediment samples (n = 89) were sampled in 2019 from the excavation's profiles (Fig. 5). In square K5; two samples were collected from a newly discovered layer, which has been interpreted in the field as a floor (L12030; Fig. 4b) of stratum 1A. This thin layer is located above Yadin's floor 5004 (our L12018, also appearing as L12040 in K7; Fig. 6), attributed to stratum 1B (Yadin, 1972). The remaining samples (n = 72) collected from the profile of K5 (Fig. 5a) showed a light grey-brown color with white and small amounts of orange-colored flakes and some mud brick remains. In square K7 (Fig. 5b), 16 sediment samples were taken from stratum 1A/B, 2, and the fill above stratum 3 (Fig. 6).

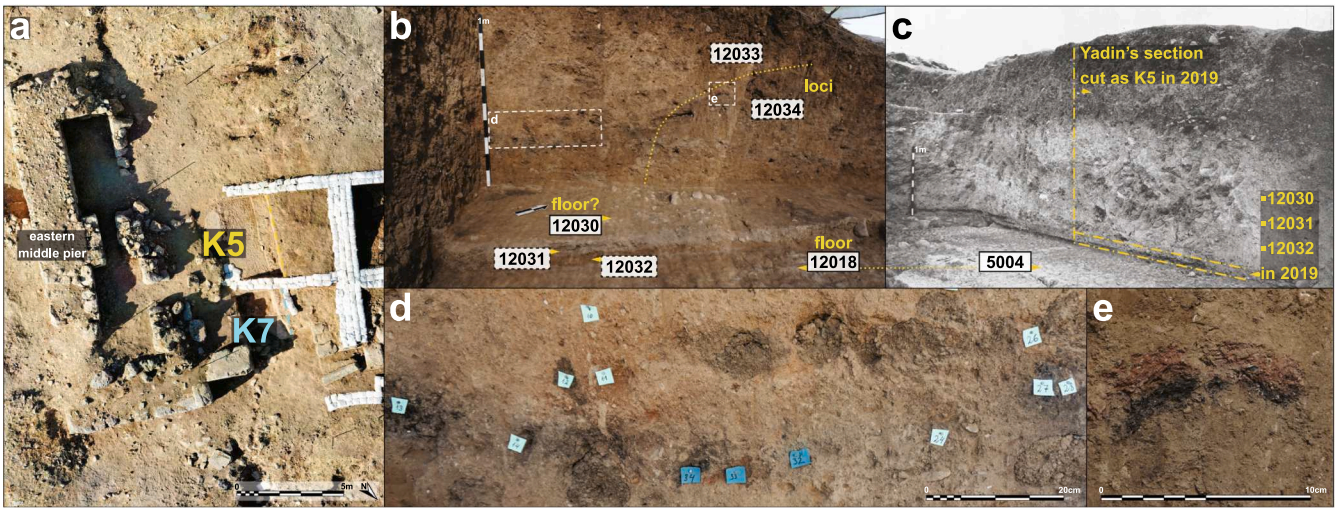

Fig. 4. Section of K5 in the gate passage. **(a)** Aerial showing gate passage during the 2019 expedition. Orange colored line indicating the section of K5. **(b)** Square K5 in 2019, looking at the sampled profile. Profile across of exposed eastern middle pier (see Fig. 4a). Showing two loci, L12033 and L12034, established during separate working days sampling the section in bulk sediments. White dotted squares show the locations of Fig. 4d-e. Below profile, at the bottom of the photograph, pebble floor L12018, corresponding to Yadin's floor 5004 in Fig. 4c. Above L12018, thin layers L12032 and L12031. Atop of that floor L12030 **(c)** The same section as in Fig. 4b photographed during Yadin's excavation and described by Yadin: "Looking north-west. Section along gate's passage-way. Below, Paving 5004 (stratum 1B). Above it, a layer of ashes and brick debris from final destruction of city-gate." (from Yadin et al., 1961: Pl. CXXXVIII:3) Note that Yadin's floor 5004 relates to floor L12018. Orange-colored lines indicating the beginning of the section continuing to the right, established in 2019 and shown in Fig. 4b. Above the pebble floor, to the right, orange rectangular patch marking the location of layers of L12030, L12031, and L12032 from 2019. **(d)** Showing burnt and grey-reddish patches within the sampled profile of 2019. **(e)** Distinct mud brick material, sample location 57. (photo a: H. Nativ; photos b, d, and e: E. Arkin-Shalev).

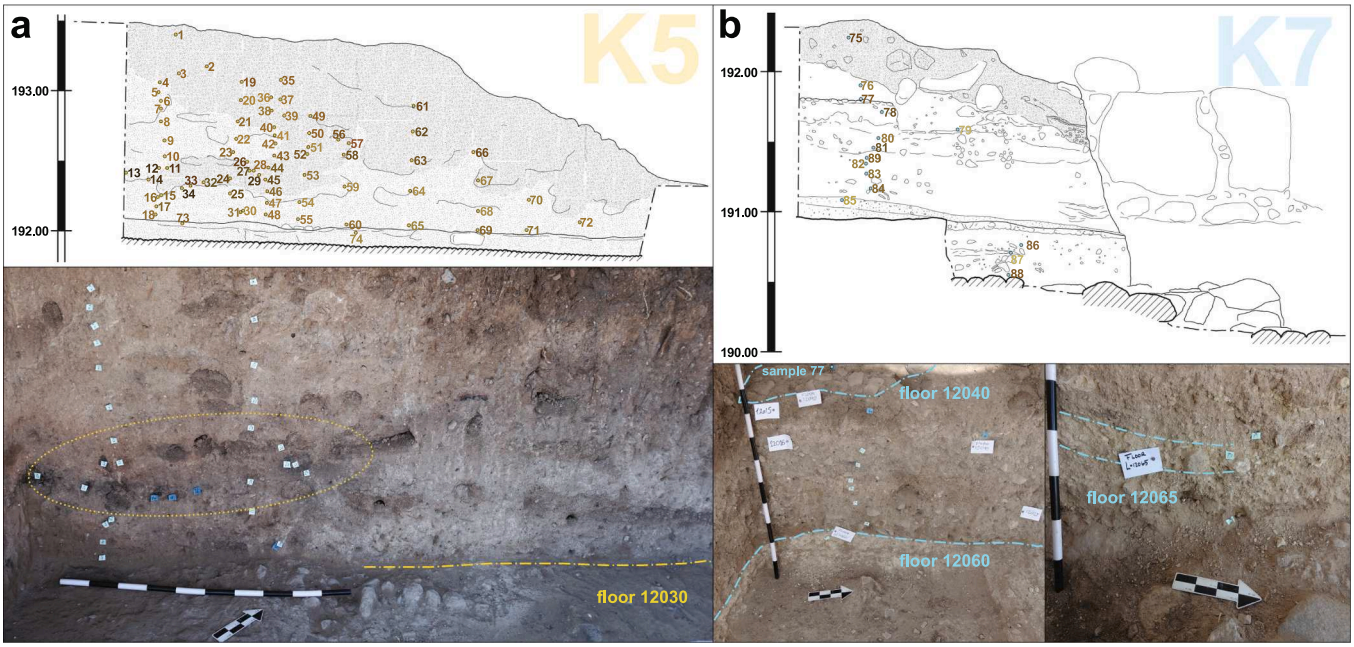

Fig. 5. Sampled sections of the 2019 expedition. **(a)** Showing the profile in square K5, including the samples in their positions following the color coding of the Munsell values taken from the macro bulk sediments (see Appendix A). Below is a photograph during the 2019 expedition, showing a systematic sampling approach in vertical columns with distinct samples taken within the darker debris (encircled). **(b)** Continuation of profile in square K7, including the samples following the color coding of the Munsell chart. Below are photographs taken during sampling. The left photo shows the upper part of the section. At the top pebble floor L12040 (encircled, Yadin's 5004) with sample 77. Below floor 12060. The right photo shows the lower part, showing floor 12065 tagged. Visible a light yellowish-brown-white stretch (adapted; drawing: S. Pirski; sketch: A. Pollack; (photos E. Arkin-Shalev)).

3.2. Methods

Micro-geoarchaeological methods, including mineralogical analysis and quantification of micro-botanical remains, were applied to understand the site formation processes and observe chrono-stratigraphic changes along Area K sedimentary sequence in relation to Yadin's interpretation of the Bronze Age gate at Hazor Lower City.

3.2.1. Mineralogical analysis via Fourier Transform Infrared (FTIR) spectroscopy

All bulk sediment samples (n = 89) were analyzed via Fourier-Transform Infrared (FTIR) spectroscopy to determine their major

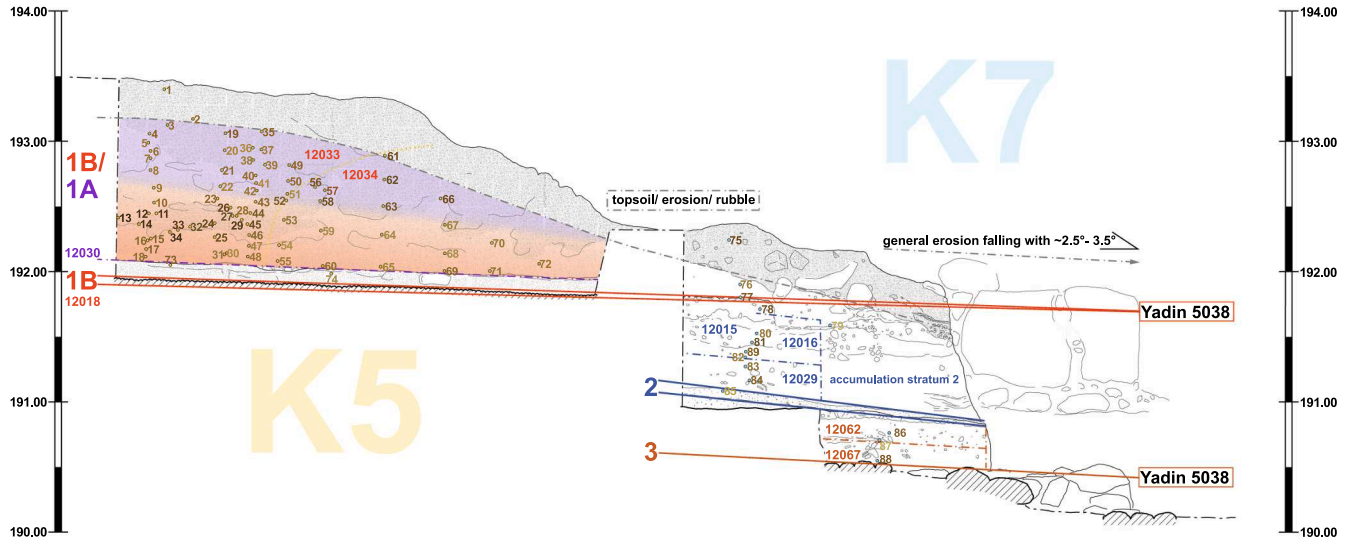

Fig. 6. Profiles of K5 and K7, showing strata 3 to 1A and the fill loci of the 2019 expedition in accordance with Yadin's stratigraphy. Yadin's floor 5038 marking stratum 3, 20–50 cm above: stratum 2 corresponding to Yadin's 5020 sounding and relative difference in elevation (Ben-Tor et al., 1989: 299). Pebble floor 5004 is distinct as stratum 1B. (adapted; drawing: S. Pirski; sketch: A. Pollack).

mineralogical composition (Weiner, 2010: ch.12). In the laboratory; the samples were divided into sub-samples (n = 167) according to different components in each sediment sample. Samples were collected using the KBr method in transmission mode between 4000 and 350 cm^{-1}, at 4 cm^{-1} resolution using a Thermo iS5 spectrometer. The collected spectra were compared to an internal library of infrared spectra of archaeological materials (the Kimmel Center for Archaeological Science Infrared Standards Library, Weizmann Institute of Science; also see Weiner, 2010).

Evaluation of clay alteration due to exposure to high temperatures (>500 °C) was based on the presence (unheated) or absence (heated) of absorption bands at 3695, 3625, and 915 cm^{-1} (following Berna et al., 2007) and the location of the main silicate absorption band (ca. 1032 cm^{-1}) plotted against the band's width (following Forget et al., 2015: Fig. 12). To evaluate the atomic order/disorder in calcite associated with its formation mechanisms (e.g., geological, biological, or pyrogenic), the ν_2 and ν_4 absorption bands, corresponding to 874 and 713 cm^{-1}, respectively, were studied by following changes in their height through repetitive grinding of samples where calcite is a major component (following Regev et al., 2010). A pre-programmed macro (using Thermo Macro Basics software) was used in order to calculate values for the height of the ν_2, ν_3, and ν_4 absorption bands of calcite, their ratio, and the full width at half maximum (FWHM) of the ν_3 absorption band following the method by Regev et al. (2010: Fig. 1).

3.2.2. *Quantification of phytoliths*

Siliceous phytoliths are biogenic minerals made of silica – the mineral opal - that form in living plants and can serve as a proxy for identifying plants (Piperno, 2006). Since phytoliths are made of durable material, they are often found in archaeological sediments to understand the use of plants and the paleo-environment (Weiner, 2010). Here, we used the rapid extraction procedure by Katz et al. (2010), applied to representative sediment samples (n = 65). Phytolith concentrations were calculated to a number of million phytoliths per 1 g sediment (M phyt/g sed) with a 30% standard deviation following Katz et al. (2010).

3.2.3. *Quantification of calcitic micro-remains*

This study aimed to analyze two types of calcitic micro-remains: wood ash pseudomorphs and animal dung spherulites (Gur-Arieh and Shahack-Gross, 2020). Wood ash pseudomorphs are calcitic micro-remains found in plant ashes (Canti and Brochier, 2017). Dung spherulites are radially forming microscopic (5–20 μm) spheres found in animal dung, especially in ruminants (Canti, 1997). These crystals and spheres can be identified under a petrographic microscope (Shahack-Gross, 2011). A selection of representative samples (n = 65) was analyzed for the concentration of their calcitic micro-remains, following the method by Gur-Arieh et al. (2013). Concentrations were calculated to a number of thousands of ash particles or spherulites per 1 g sediment (e.g., k ash/g sed) with a 30% standard deviation following Gur-Arieh et al. (2013; see also Gur-Arieh and Shahack-Gross, 2020).

4. Results

The results of the microscopic analysis, including FTIR and quantification of phytoliths, wood ash pseudomorphs, and dung spherulites, are summarized in Appendix A.

4.1. *FTIR*

Overall, all 167 spectra produced from 89 sediment samples showed high similarity in their major mineral composition. The sediments of Area K are mainly composed of calcite, clay minerals, and quartz (Fig. 7). Calcite was identified through its main absorbance bands at 1429, 875, and 713 cm^{-1} (Weiner, 2010: 284). The prominent absorbance bands for clay were identified between 1042 and 1030 cm^{-1}, the distinctive hydroxyl absorbance bands at 3695 and 3625 cm^{-1} and minor absorbance bands at 917 and 528 cm^{-1} (Weiner, 2010: 302). A shoulder determined the presence of quartz in the main silicate absorbance band at 1084 cm^{-1} and a relatively high characteristic doublet at 798 and 778 cm^{-1}, and a minor band around 695 cm^{-1} suggesting moderate amounts of quartz in most sediment samples (Weiner, 2010: 299).

Based on the mineralogical analysis, the samples were divided into four groups: (1) sediments with clay and calcite in relatively similar amounts; (2) clay-rich sediments; (3) calcite-rich sediments; and (4) sediments composed almost entirely of calcite (Fig. 6). Analysis of clay exposure to elevated temperatures showed that out of the 89 sediment samples, only 19 samples could be attributed to having been exposed to heat above 500 °C, though probably lower than 700 °C (Fig. 8). The interpretation of burnt clay followed Berna et al. (2007) and Forget et al. (2015), including the shift of the main silicate absorption band at around 1035 cm^{-1} and the absence of the peaks around 3695, 3625, and 915

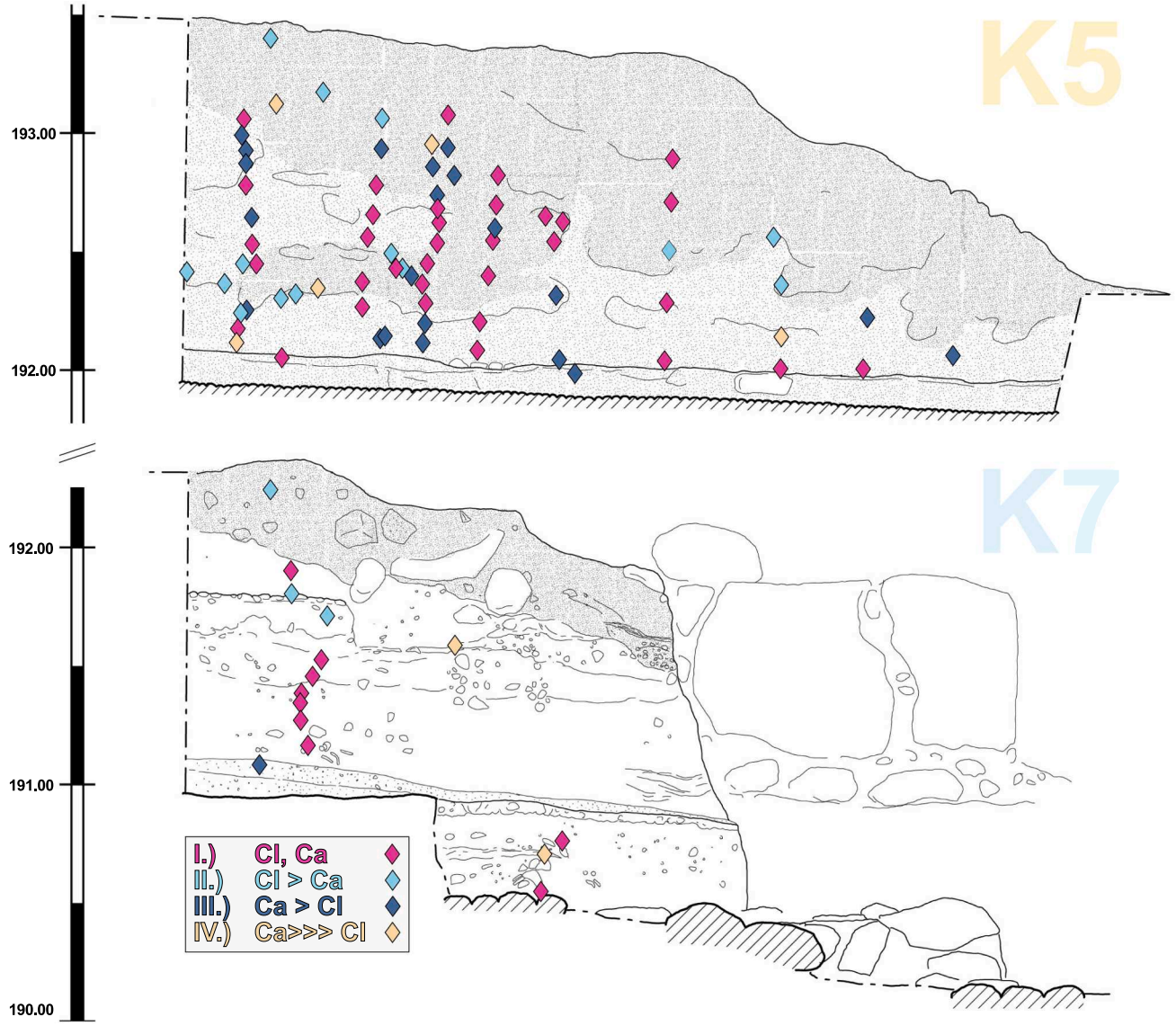

Fig. 7. Mineralogical composition within the sections of K5 and K7 in four groups: I) sediments with clay and calcite in relatively similar amounts, II) clay-rich sediments, III) calcite-rich sediments, and IV) sediments composed almost entirely of calcite.

cm^{-1} (Fig. 9). Based on the above we divided clay minerals to three categories: non-altered (n.a.), altered (a.) or slightly altered (s.a.) in case the above indicators were not very clear. In the vicinity of those samples where the clay has been distinguished as altered, several other samples contained low amounts of small orange flakes (Fig. 8b). Those were marked within the sequences as altered flakes found within samples 2, 18, and 35 (Appendix A).

In order to detect the atomic order/disorder in calcite as a proxy for its pyrogenic origin (Chu et al., 2008; Regev et al., 2010; Poduska et al., 2011), 60 grinding curves, following Regev et al. (2010) were created from sediment samples rich in calcite. The plots show that all of the calcitic samples are only slightly disordered. The calcite-rich spectra generated in this study were compared to the reference library (Kimmel Center for Archaeological Sciences, Weizmann Institute of Science), which could have a geogenic origin but perhaps also derive from wood ash.

4.2. Phytoliths

Extraction and quantification of phytolith concentrations were performed on 60 sediment samples (Fig. 10a). Out of this total, 18 samples showed low concentrations of phytoliths ranging between 0.3 and 1 million phytoliths in 1 g of sediment (M phyt/g sed). 13 of these samples derive from the southern, thicker area of K5 (Fig. 8b). Five are distributed throughout the profile of K7 (Fig. 8b). The analysis was based on relative differences. Topsoil provided no archaeological output and showed very low concentrations, sample 1 being considered a control.

Another group of 32 samples presented 1 to 3 M phyt/g sed concentrations. These samples appear within both sample locations (K5 and K7). The last group of 10 samples displayed the highest abundance with over 3 M phyt/g sed. Of this group, nine are between 192.0 and 192.5 mamsl—one in K7 and eight within K5. One sample (83), with concentrations of 4.8 M phyt/g sed, is located in the middle sequence of K7, at 191.4 mamsl. The samples of the group rich in phytoliths located in K5 form two bands with a stretch of samples with lower concentrations of phytoliths in-between (Fig. 9; Appendix A). During the analysis, fully preserved and fragmentary phytoliths were observed (Fig. 11a).

4.3. Ash pseudomorphs and dung spherulites

The extraction and quantification of calcitic micro-remains focused on wood ash pseudomorphs and dung spherulites applied to 60

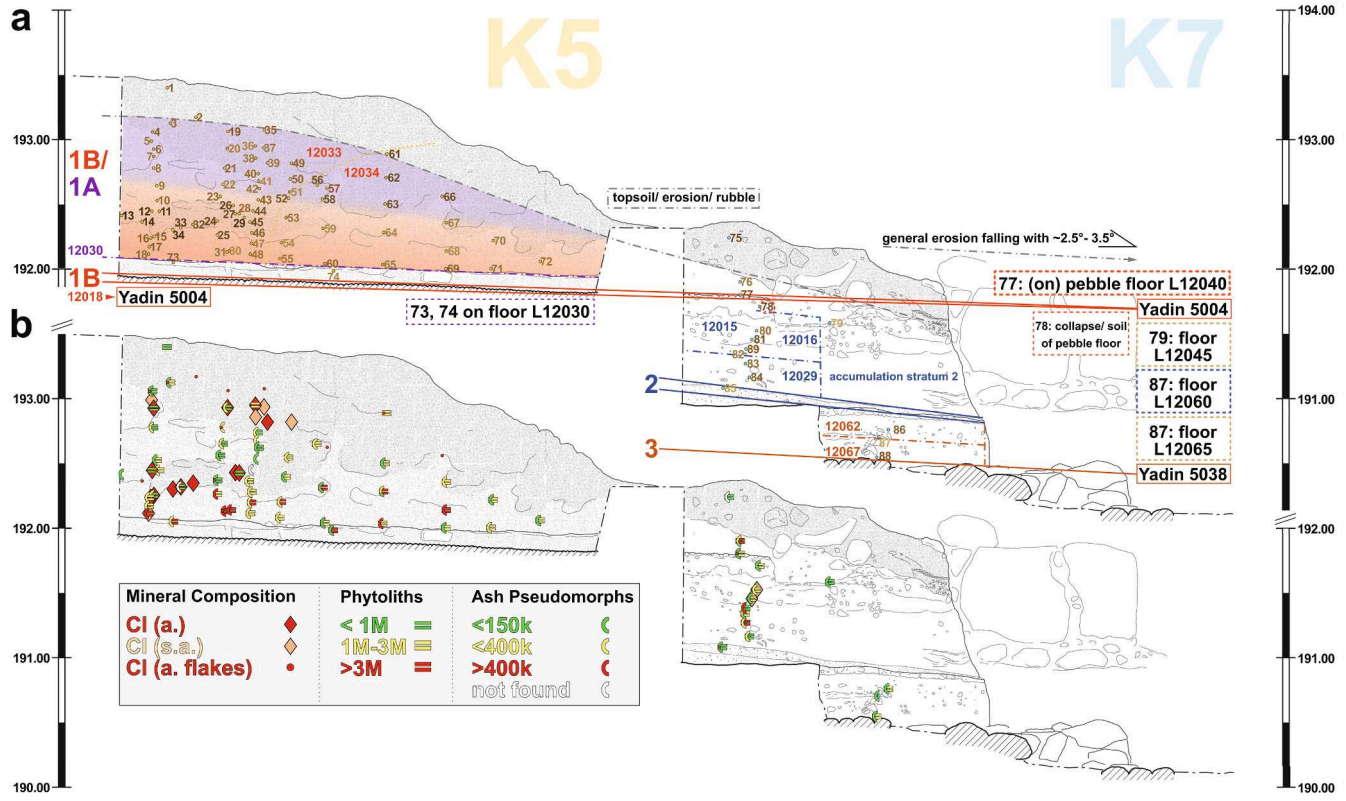

Fig. 8. Profiles in squares K5 and K7. **(a)** Showing the stratigraphy from 2019 combined with Yadin's designation. Samples designated to floors and strata in K7: 88 atop Yadin's 5038; 87 from floor L12065, probably Yadin's paving 5002; 85 from floor L12060; 85 from floor L12060 corresponding to stratum 2. 79 from floor L12045. Sample 78 as part of the collapsed pebble floor L12040, Yadin's 5004. 77 from the pebble floor itself. In K5, samples 73 and 74 are from the new layer L12030. **(b)** Samples with full integration of the results. They are composed of heated clay, three distinguished groups of phytoliths with natural/ non-anthropogenic abundance in green, relative intermediate amounts in yellow, and the highest abundance in red. In relative comparison, the concentrations of ash pseudomorphs are displayed within the three groups of low, intermediate, and high signatures.

representative sediment samples (Fig. 10b; Fig. 11b-c). The results show the occurrence of ash pseudomorphs throughout both squares (Fig. 8b). 24 of the 60 samples have concentrations of up to 150 thousand ash pseudomorphs per 1 g of sediment (k ash/g sed). Seven samples show an abundance above 400 k ash/g sed, with maximum concentrations reaching 540 k ash/g sed.

The other 29 samples show concentrations in-between those two groups (150–400 k ash/g sed). In K5, the ash pseudomorphs appear in the highest abundance above the floor level in this square (L12033). These samples compile within a 30 cm thick layer along the whole section of K5 (Fig. 8a). Within K7, only one sample shows a high concentration of ash pseudomorphs with 401 k ash/g sed.

No dung spherulites were found in any of the studied samples. Spherulitic features within the sediments were interpreted as coccoliths abundant in the regional chalk.

5. Discussion

5.1. Stratigraphy and formation processes

In this study, we aim to use the micro-geoarchaeological data to understand better the formation processes within the gate complex of Area K in Hazor. The FTIR analysis shows that the major components of the sediments in this area are clay, calcite, and quartz, as found in the region's soil (Singer 2007). Furthermore, analysis of the atomic order of calcite indicates its geogenic origin alongside coccoliths that indicate an abundance of chalk. This data corroborates with the regional geological Hazor-Gadot formation composed of chalk and conglomerate (Geological Survey of Israel 2016). Signs of fire residues were found within the studied sediments in the form of altered clay and microscopic identification of calcitic wood ash pseudomorph particles. In addition, the sediments exhibit moderate amounts of botanical remains due to human activity identified in the form of phytoliths. Below we discuss the variability in the sediments' mineralogy and concentrations of micro-remains as a proxy for human activity and site formation processes according to their archaeological context.

5.1.1. Square K7

Stratum 3. Within the deposit at the bottom of square K7, between 190.46 and 190.76 mamsl, three samples display the layers accumulated atop stratum 3 (following Yadin's stratification, Fig. 8a-b). The top and bottom samples (88 and 86) are characteristic of an even mix of clay and calcite. Sample 87 appears white-yellowish in color and is composed of calcite, which seems to be chalk. The top samples (86 in L12062 and 87 from L12065) present low concentrations of ash pseudomorphs and phytoliths, and sample 88 in L12067 at the bottom shows slightly higher concentrations (205 k ash/ g sed and 1.1 M phyt/ g sed). Overall, stratum 3 in square K7 displays unaltered clay and calcite, indicating human activity with a relatively low signal.

Stratum 2. Sample 85 in locus L12060, at around 191 masml, is attributed and recognized as Yadin's floor (5020) of stratum 2. This yellowish-white layer consists mainly of calcite, despite a small reddish flake being exposed to heat (possibly a pottery fragment). Like the deposit beneath (in stratum 3), ash pseudomorphs and phytoliths are found in low concentrations (<150 k ash/ g sed; phytoliths < 1 M phyt/ g sed). Atop this floor, the next span of layers, locus L12029 and L12016, up until the pebble floor of stratum 1B, accumulates to a height of 191.61 mamsl. A balanced mix of clay and calcite characterizes these

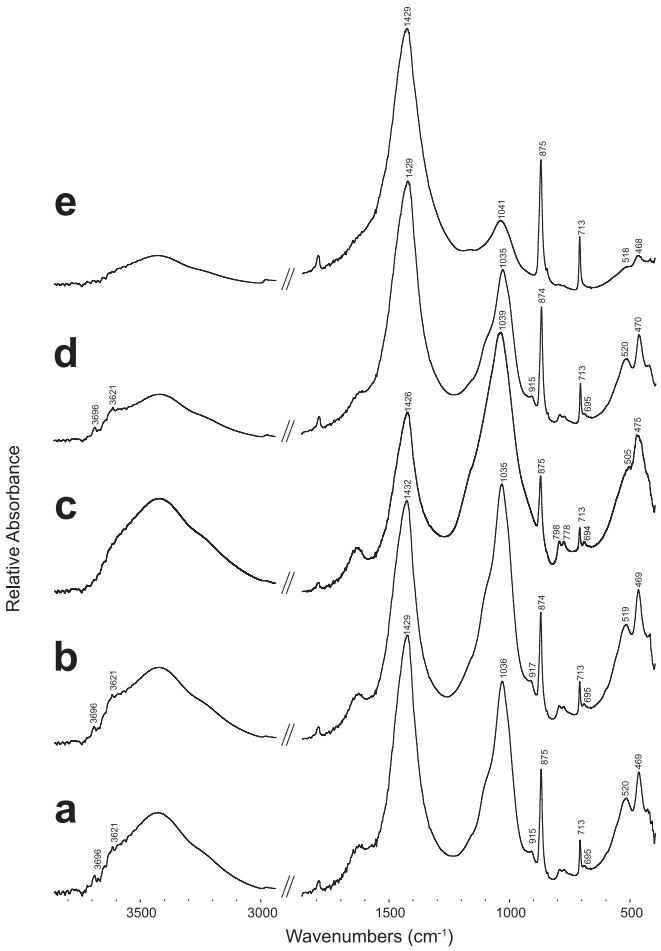

Fig. 9. FTIR spectra of five samples attributed to the four groups: I) sediments with clay and calcite in relatively similar amounts, here a) and b); for a), note the absence of the absorption bands at 3695, 3625 and 915 cm^{-1} II) clay-rich sediments, here c)- note that the clay here is altered; III) calcite-rich sediments, here d); IV) sediments composed almost entirely of calcite, here e).

layers' six samples (80–89). The clay component in the lower four samples (84, 83, 82, and 89) shows no evidence of exposure to heat. In the two upper samples (81 and 80), the FTIR analysis indicates the presence of slightly altered clay with intermediate concentrations of ash pseudomorphs (<400 k ash/ g sed), as well as phytolith concentrations (up to 3 M phyt/ g sed).

Two samples (89 and 83), located below the samples of slightly altered clay, stand out with high amounts of micro-remains. Sample 89, below sample 81, provided 401 k ash/ g sed, with a lower concentration of phytoliths (0.8 M phyt/ g sed), compared to the rest of the samples in this locus, which might indicate the burning of wood, which do not produce high amounts of phytoliths (Tsartsidou et al., 2007). In contrast, in sample 83, located below sample 89, up to 4.8 M phyt/ g sed are determined. While sample 89 is rich in wood ash particles, the ash concentration in sample 83 is significantly lower (241 k ash/ g sed). In locus L12045, situated further to the right in the section, at 191.60 mamsl, corresponding to Yadin's stratum 2, sample 79 was taken from yellowish-white sediment. While it is mainly composed of calcite, this sample has low amounts of both micro-remains, typically indicating chalk deposition.

Stratum 1. Sample 77 (at 191.75 mamsl) in locus L12040, taken on top of the pebble floor of stratum 1B, is a typical mix of clay and calcite. In this sample, red flakes of burnt clay are evident, probably originating from pottery fragments. It also contains small amounts of ash, with a 60 k/ g sed concentration. Phytolith abundance is around 1.4 M phyt/ g sed. Sample 78, found slightly below, shows high similarity in composition and micro-remain concentrations, as on the floor.

The excavation profile in square K7 continues up to 192.4 mamsl. In the upper locus, L12014, the two sediments sampled display the typical composition of clay and calcite but differed drastically one from the other in their amounts of micro-remains. The lower sample (76) shows a high abundance of phytoliths (3.6 M phyt/ g sed) and some amounts of ash (168 k ash/ g sed). No ash pseudomorphs are identified in the topmost sample (75), which appears darker than the samples below it. The abundance of phytoliths is below 1 M phyt/ g sed. This layer is very close to the surface and might represent a more recent deposition.

5.1.2. Square K5

The section exposed in K5 is representative of stratum 1 (Fig. 8a-b). The excavation profile in this square presents the destruction debris described by Yadin as two loci (L12033 and L12034) which we divided into seven different layers (I-VII), some showing internal division (Fig. 12). Below, the descriptions of the layers are ordered from bottom to top.

(I) At the bottom of the profile, two samples (73 and 74) were sampled on top of layer L12030, resting on the pebble floor. Their composition is mainly clay, quartz, and calcite. Both samples observe high phytolith concentration (3.5–3.7 M phyt/ g sed), while these samples contain some ash (343 k and 59 k ash/ g sed). The samples above layer (I), at 192.05 mamsl, span over a height of over 1 m. Most of the samples are characteristic, consisting mainly of clay and calcite.

(II) Locus L12033 (see Fig. 4b.; Fig. 8; Fig. 12a), located right above the pebble floor (sample 73), displays debris of around 40 cm long dominated by clay-rich sediments that, according to the FTIR analysis, have been exposed to heat. Below is the detailed description of layer II based on internal division:

- (II-m) A 20 cm thick layer where clay shows evident alteration due to exposure to elevated temperatures (samples: 12, 15, 16, 27, 28, 32, 33, and 34). These samples are most likely the result of burnt mud brick accumulation.
- (II-ap) Underneath the mud brick layer, the highest ash and phytolith concentrations are observed (>400 k ash/ g sed; > 3 M phyt/ g sed). However, the clay component is not altered, although some burnt clay flakes are identified. The sediments, rich in micro-remains, spread like the mud brick layer (II-m) and span horizontally in locus L12033. These might represent an activity surface or an accumulation prior to the burnt mud brick debris (Friesem et al., 2014; Regev et al., 2015).
- (II-p) Slightly higher in the profile, at the level of the burnt mud brick debris (II-m), this context is characterized by high phytolith concentration that stretches throughout locus L12034 (Fig. 4b.; Fig. 8; Fig. 12). Ash appears in intermediate amounts (143–200 k ash/ g sed) (Appendix A).
- (II-a) Above the layer atop the pebble floor within the profile of locus L12034, two samples below the phytolith-rich horizon (II-p) of locus L12034 align on the same level with the ash and phytolith-rich samples of locus L12033 (II-ap). Ash concentrations in samples 65 (421 k ash/ g sed) and 68 (440 k ash/ g sed) are relatively high.
- (II-pl) A context found below the phytolith-rich layer (II-p) and surrounding the layer (II-a) is characterized by intermediate amounts of ash and phytoliths. These might represent occupation deposits on the floor mixed with some collapsed construction materials.

This stratigraphic sequence showing a floor (I) overlain by a wood ash-rich layer (II-a) below a phytolith-rich horizon (II-p), then sealed by an accumulation of mud brick debris (II-m), could represent a floor-roof complex (cf. Friesem et al., 2014) made of a thatch roof (phytolith-rich) over roof wood beams (rich in wood ash pseudomorphs) within a mud

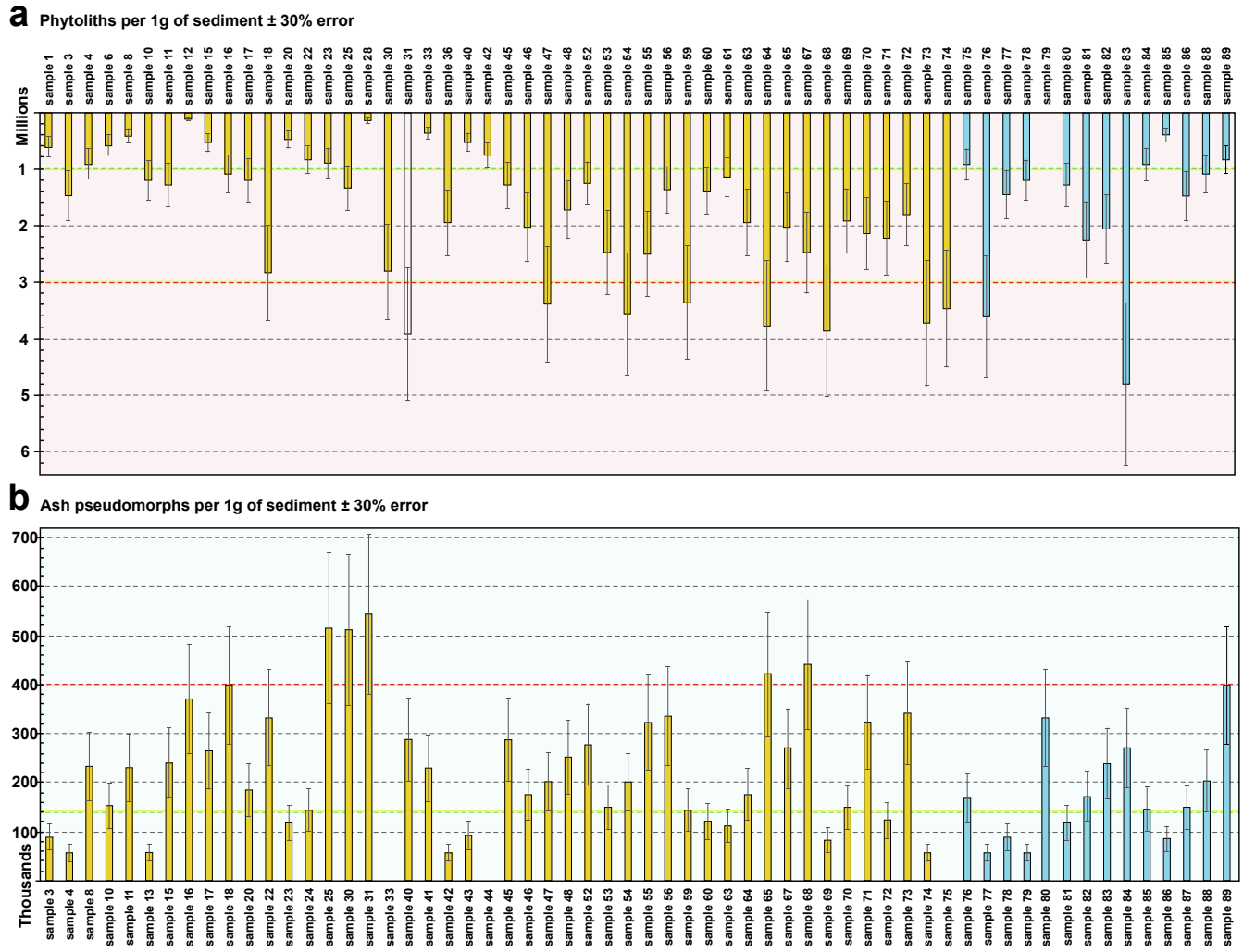

Fig. 10. Showing results of quantified micro-remains within 60 samples from K5 (orange) and K7 (blue). **(a)** The concentration of phytoliths in millions per 1 g of sediment, including the ± 30% error margin resulting from the rapid extraction method by Katz et al., 2010. Distinguished groups of phytoliths with natural/ non-anthropogenic abundance in green below 1 million, relative intermediate amounts in yellow between 1 and 3 million per 1 g of sediment, and the highest abundance in red with concentrations above 3 million per 1 g of sediment. **(b)** The concentration of ash pseudomorphs in thousands per 1 g of sediment, including the ± 30% error margin resulting from the rapid extraction method formulated by Gur-Arieh et al., 2013. Low abundance in green below 150 thousand, relative intermediate amounts in yellow between 150 and 400 thousand per 1 g of sediment, and the highest abundance in red with concentrations above 400 thousand pseudomorphs per 1 g of sediment.

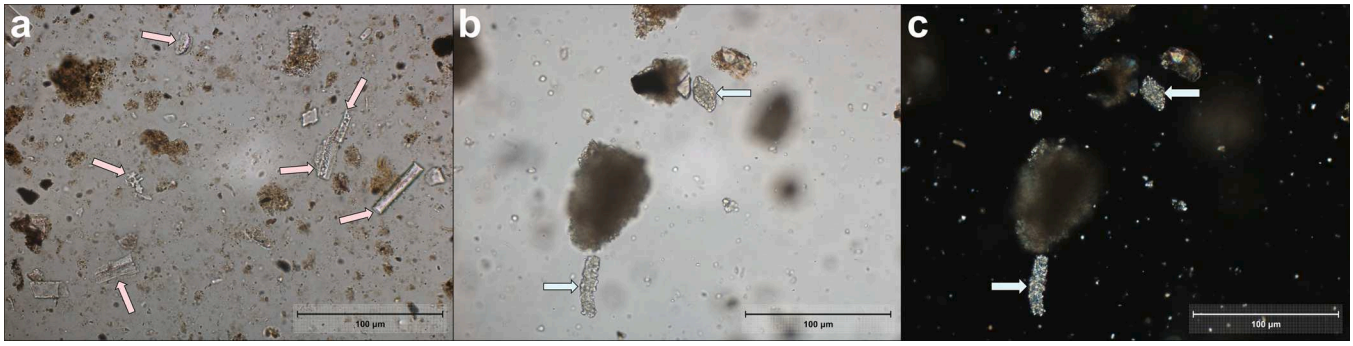

Fig. 11. Showing micro-remains from sample 55. **(a)** High concentration of phytoliths (light pink arrows) within the sample under x400x magnification. **(b)** Two ash pseudomorphs (light blue arrows) under x400 magnification, taken under PPL. **(c)** Two ash pseudomorphs (light blue arrows) under x400 magnification, taken under XPL.

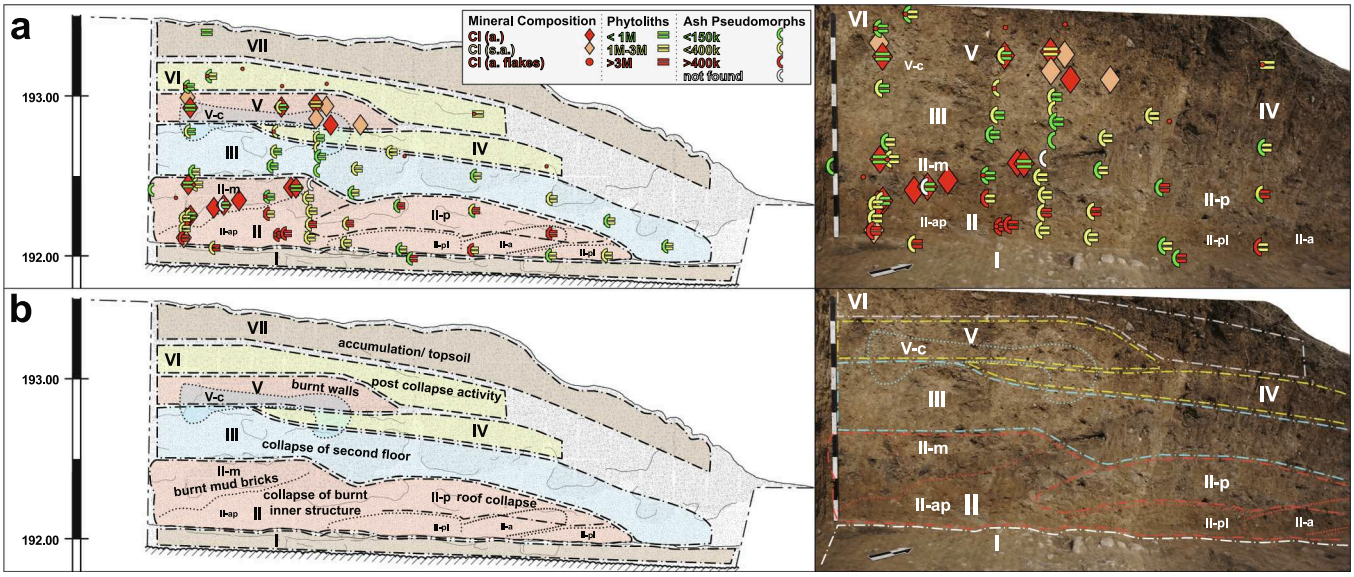

Fig. 12. The section of square K5. **(a)** Description and Interpretation on the left with the profile of the 2019 expedition on the right (see discussion 5.1.2) **(b)** Layers as interpreted in discussion with the 2019 section on the right (5.2.).

brick structure. The presence of mud brick debris (II-m) at one side might indicate the proximity of the wall as opposed to the central part of the structure (II-p/II-a) (Friesem et al., 2011; 2014).

(III) The accumulation of mud brick and micro-remains showing signs of burning is overlain by a layer (30 cm thick) found at 192.50 mamsl, which forms part of locus L12033. This layer does not provide any indication of exposure to heat and contains, in comparison to the layers beneath it, lower amounts of phytoliths (<2.5 M phyt/ g sed) and wood ash (<331 k ash/ g sed). With a well-preserved piece of mud brick found in sample 57 (Fig. 4g), this layer probably represents sedimentation attributed to non-recurring human impact (e.g., building installations) with a low signal of human activity. This layer thins above the phytolith-rich layer of locus L12034, aligning with the natural slope (Fig. 12).

(IV) In locus L12033, at 192.80 mamsl, intermediate ash concentrations can be observed, while the sediments contain little red flakes, which were exposed to heat but could be the remains of pottery fragments. Overall this layer is similar to the one below (III) but might indicate an increase in human activity deposition, as evidenced by the elevation of ash and the presence of pottery fragments.

(V) Five to ten centimeters above layer (IV), in locus L12033, a 20 cm thick sediment indicates clay alteration due to exposure to high temperatures. It contains intermediate amounts of phytoliths, with similar amounts of ash, as the stretch beneath (IV). Considering its mineralogical composition showing evidence of burning, we interpret this layer as burnt mud bricks. Within this layer, reaching into (III) and (IV), some sediments differ in their composition showing calcite-rich composition (V-c) with lower to intermediate concentrations of phytolith and ash (Appendix A).

(VI) Sediments in this layer contain little red flakes of altered clay and low to moderate amounts of phytoliths (<1.5 M phyt/ g sed) and some ash pseudomorphs (<90 k ash/ g sed). The mineralogical compositions of the sediments range between different amounts of clay and calcite (Appendix A).

(VII) The top-most 10 cm of the profile is defined as a sediment layer with low concentrations of phytoliths and ash compared to the sediments below. Thus, this layer represents a very low signal of human activity and probably reflects a post-abandonment deposition.

5.2. *Archaeological implications*

The vast majority of samples display a composition prevalent in tell sites in the Southern Levant dominated by clay, calcite, and quartz and with variable amounts of pottery fragments and high to moderate (above natural accumulation) concentration of phytoliths and wood ash pseudomorphs (e.g., Shahack-Gross et al., 2005; Namdar et al., 2011; Regev et al., 2015). The identification of specific contexts where the clay has been altered due to exposure to elevated temperature, as well as deposits rich in wood ash pseudomorphs and phytoliths, may indicate burning events (e.g., Berna et al., 2007; Namdar et al., 2011; Regev et al., 2015), which we interpret here, as the debris of a burnt structure (including mud bricks, roofs, and floors), most likely the gate complex. Nevertheless, variability in micro-remains found within the sediments can be used as a proxy for shifting intensities of human activity and different construction materials. Thus, based on the micro-archaeological record, we provide below a new interpretation of Area K strata.

The excavation campaign of 2019 re-identified the architectural layout of the gate and its associated stratigraphy provided by Yadin (see Fig. 8a; Yadin, 1972: 58-63; Ben-Tor et al., 1989: 297; Ben-Tor, 1993: 599). Based on the micro-geoarchaeological analysis of the sediments and their stratigraphic context, we interpret Yadin's strata from bottom to top.

Stratum 3. The gate of this stratum dates to the late MB II. Three pilasters were discovered throughout the passage, narrowing its width to 3 m. A fortification system of several rooms was documented (Yadin, 1972: 60,61; Ben-Tor et al., 1989: 280-284; Ben-Tor, 1993: 599). Yadin associated a solid stone floor (our sample 88 in fill L12067) with locus 5038 and 5020/1 (square K7) he attributed to stratum 3, which he viewed as the floor of the MB II-C gate (Yadin et al., 1961: Pl. CXXXIII: 1; Ben-Tor et al., 1989: 282). Overall, our results might be viewed as confirming this interpretation by exhibiting moderate wood ash remains and phytolith concentrations, which tend to be deposited on top of occupation surfaces (e.g., Shahack-Gross et al., 2005; Namdar et al., 2011; Friesem et al., 2014; Regev et al., 2015). Stratum 3 presents a continuous occupation with a deposit which shows an accumulation of 0.5 m made of two main episodes of occupation surfaces/floors (sample 88 in fill L12067 and sample 87 from the surface of L12065, Yadin's paving 5002, Yadin et al., 1961: Pl. CXXXIV: 1). The latter consists mainly of calcite without phytoliths. Since the calcite does not indicate a

pyrogenic origin, it might be associated with non-pyrogenic pulverized chalk plaster, as reported at Tel Kabri (Goshen et al., 2017; see also Friesem et al., 2020). Above the floor, sediments contain low concentrations of ash and moderate ones of phytoliths (0.5 – 1.1 M phyt/ g sed and 150–401 k phyt/ g sed), as sediments continued to accumulate, possibly as human activity continued until the deposition of stratum 2. However, it is also possible that the sediments above stratum 3 floors and the bottom part of stratum 2 were deposited intentionally as part of the preparation for the floor of stratum 2, i.e., constructional fill using the tell sediments to raise the level of the passageway in the gate.

Stratum 2. The gate in this stratum was built during the LB I and was erected upon the structures of the stratum 3 gate. A raising of 0.3 m on the previous stratum was noted, and the gate's exit paved with large basalt stones was reported (Yadin 1972: 62; Ben-Tor et al., 1989: 285; Ben-Tor, 1993: 599).

The floor of stratum 2, L12060 (Yadin 5020), forms a 15 cm thick deposit and shows similar attributes as the stratum 3's plaster floor (L12065) mentioned above. On top of it, the wet and dry sieving of locus L12016 resulted in numerous small pottery sherds, animal bones, and fish vertebrae (G-86/2019; Arkin-Shalev, 2019: 4). A similar layer was observed in Tel Dor's area D2, associated with fish processing activity on and in-between plaster floors (Shahack-Gross et al., 2005: 1421, 1428). While in Tel Dor, such remains as fish bones are common due to their vicinity to the sea, layers L12029 and L12016 in square K7 are inland and at the gate's entrance. The sediments of these loci are above the stratum 2 floor and show fluctuating concentrations of phytoliths and ash ranging between 0.8–4.8 M phyt/ g sed and 117–401 k phyt/ g sed, respectively. In the upper locus L12016, we identified a sedimentary sequence associated with burnt debris (samples 80, 81, 82, 83, and 89). Sample 82 contained an opal signature within the FTIR spectrum, which indicates a high concentration of opaline phytoliths (Shahack-Gross et al., 2005: 1423). With an intermediate concentration of 2 M phyt/ g sed, the appearance of opal as such suggests typical tell site remains (Albert et al., 2008: 17). Thus, we interpret this sediment, including the fish bones, as either an intentional fill to provide the foundations for constructing the LB II gate of stratum 1B or potentially depositions of human activities. In addition, Yadin noted above stratum 2 the raising of floors for 1B within the gate's passage (Yadin, 1972: 62; Ben-Tor et al., 1989: 287). Above L12016, Locus L12045 is once again very similar to the L12065 but appears as a small layer. The results show a very calcite-rich layer, which we interpret as a potential floor (Shahack-Gross et al., 2005). This layer could also be stabilizing the foundation plateau of the pebble floor. While the locus does not extend further south into the passage, it is less likely to correlate with another walking horizon.

There is only one vertical sample set, so it is not easy to ascertain this layer's depositional process. Nevertheless, the wet sieving residues from 2019 mentioned above make preparing the ground for another floor or reconstruction of the gate in stratum 1B more probable.

Stratum 1. Yadin's pebble floor 5004, assigned to stratum 1B, was identified in squares K5 and K7.

While sample 77 (K7) was taken at 191.73–191.79 mamsl, sample 74 (K5) was taken directly on L12030. Sample 74 is 0.1–0.15 m above the pebble floor of L12040 (L12018 in K5). However, the elevation of L12030 can still be correlated with its extension above L12040 in K7.

Readdressing the architectural features briefly, the layers attributed in the loci L12033 and L12034 of K5 will be framed in their archaeological context. Envisioning the massive, multi-leveled mud brick gate structures of the Late Bronze Age (Biran 1994; Burke 2008; Stager et al., 2018), the gate in Area K had three piers, each of 3 m in length on both sides of the passage. At the entrance, those piers narrowed the passage to a 3.1 m. The middle pier cut the passage to 3 m (Ben-Tor et al., 1989: 287). These piers likely served for installations of mud brick arches containing wooden beams, which supported the ceiling's vaults as buttresses (see Yadin 1959: 9; Burke 2008: 61; 70; Stager et al., 2018). This construction held the roof and possibly an upper floor of the gate. Note that a potential second floor was also suggested for the LB I-II gate of Area P, where walls found within the southwestern gate chamber, L.1414 were interpreted as such (Ben-Tor et al., 1997: 355). The upper

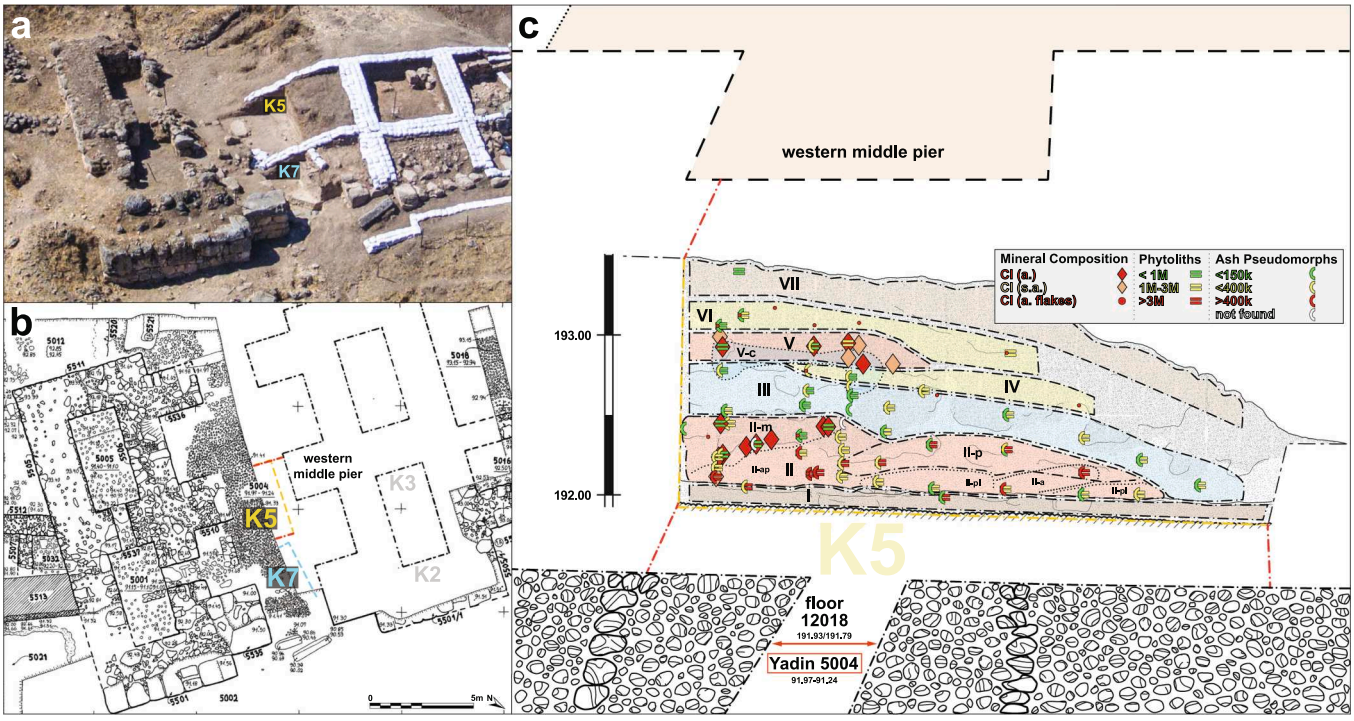

Fig. 13. The sequence of square K5. **(a)** Aerial at the end of the 2019 expedition, showing the K5 section. **(b)** Stone plan of 1958 stratum 1B with K5 in the extension of the middle pier. **(c)** The interpreted sequence of K5 with micro-remains placed into the stone plan of Yadin's 1B. Elevations for L12018 (2019) and 5004 (1958) are provided. Dotted pink lines indicate the indention of the 2019 excavation, assuring a well-preserved context. The red line indicates the distance to the western middle pier. (photo a: H. Nativ).

floor was likely not solely made of mud- bricks and thatch but enforced by cross-beams for more stability to support the walking horizon (e.g., vaults found in Ashkelon, see Stager et al., 2018).

Placing the sequence of K5 (Fig. 13a-c) within the structures of the former gate (Fig. 13c), the layers distinguished in Fig. 12a. suggest a possible scenario for gate destruction and the accumulation of its debris atop floor L12018/ L12040 (Yadin 5004).

Unfortunately, we do not have data from L12032 and L12031 (Fig. 4; Fig. 8), the accumulation above of L12018 (layer I in K5) or 12,040 (in K7), which leaves us with two different yet close interpretations:

- (a) An additional floor level (L12030), which was not mentioned by Yadin. The 2019 expedition suggested this interpretation (G-86/2019**;** Arkin-Shalev, 2019).
- (b) A make-up on top of Yadin's floor 5040 (L12018, L12040). An explanation for this accumulation of L12030 could be seen as a phase of decline in the city, in which the pebble floor itself was no longer maintained.

However, both possibilities do not hinder this study's main conclusion, that the last gate phase in Area K was destroyed in a major conflagration. In addition, in light of the macro-archaeological observations, both options suggest reconsidering the sub-divisions suggested in 1989 (Ben-Tor et al., 1989: 297).

The phase of this destruction within stratum 1 cannot be entirely ascertained, as it may await further study. Nevertheless, based on our results, we suggest the following scenario:

The phytolith-rich samples (73 and 74) at the top of layer I and visible burnt patches support the burning which would have occurred during the period of use of the gate, either as part of the gate burning down or due to human activity.

However, layer II shows more apparent indications for the collapse of the gate complex due to conflagration as evidenced by its indicative stratigraphic sequence (Fig. 12b):

- First, at the bottom of the sequence (II-ap), these indications for burnt wood deposits are interpreted to represent the collapse of the wooden arches supporting the ceiling vaults, which burnt down.
- At the same level (II-pl; II-a; II-p), high concentrations of ash and phytoliths might be attributed to collapsed thatch and wood, such as cross-beams, which burnt down as the ceiling caught fire and then collapsed on top of the floor.
- On top of the collapsed roof deposits, we found debris of burnt mud bricks (II-m), at the edge of the profile in the extension of the middle pier, thus, possibly indicating the collapsed interior mud bricks of the ceiling.

A tentative scenario for this destruction sequence (II) assumes that the fire started inside the gate, as we identified burnt mud bricks (II-m) only on the part of the profile. The wooden arches supporting the vault probably caught fire first, as studies showed that mud brick walls are less likely to be ignited first, while thatch roofs and wood beams are usually the first to catch fire (Friesem et al., 2014; Kreimerman and Shahack-Gross, 2019). This interpretation is also supported by the stratigraphic location of (II-ap) and (II-a) resting below the burnt mud brick debris (II-m).

As the roof was set on fire and collapsed, mud bricks were exposed to the fire (II-m). However, the second-floor walls, including the parts of the passage's ceiling, were not affected by the heat and eventually accumulated on top of the burnt residues (III). Presuming a second floor, the ceiling would have been thickly constructed. The speculative cross-beams (II-p) seem reasonable for a thick second floor.

Dothan *et al.,* noted floor remains in 1A (Ben-Tor et al., 1989: 296), which we suggest could likely be attributed to this layer (III). Alternatively, this layer (III) could represent a phase of post-abandonment sedimentation, given the low signature of human activity in this layer. However, considering the mud brick, the immense size of the gate, and potential second-floor use, we tend to interpret this layer (III) as unburnt debris of the upper floor (Namdar et al., 2011: 3475–3476).

The overlain layer (IV) seems to show high similarity to layer (III) but with some pottery fragments at its top.

As opposed to those layers (III and IV), layer(V) shows burnt mud bricks, whereas the sediments in (V-c) are calcite-rich. As in layer (III), the mud bricks align in the elongation of the rusticated ashlar in the middle of the gate passage (see Fig. 13; also visible in Fig. 2).

Therefore, following the scenario described throughout the previous layers, a possible explanation for this accumulation would be the attribution to the burning of the inner walls, which were exposed to the fire as the roof burnt out. The calcite might be representative of plaster, such as the plastered seams in Ashkelon (phase 13C) visible on the ashlar pier 120 (e.g., Stager et al., 2018: 52, fig. 2.36) or burnt wood ash (from potential beams), as part of the walls (V-c) fell into layers (IV) and (III). After the collapse of layers (II), (III), and (IV), the walls left without a roof and exposed to the elements started to deteriorate and accumulate on top of the floor-roof deposits (Friesem et al., 2014).

On top of the gate debris, we interpret layer (VI) as a phase of low human activity (e.g., Albert et al., 2008) based on low to moderate phytolith and ash abundance with some altered flakes, possibly from pottery sherds. Based on stratigraphic relations only (in the absence of datable material in this area), this layer (VI) could be assigned to represent the period of stratum 1A or later.

Sealing the sequence, layer (VII) continues into K7 and shows lower signals than its underlying layer (VI), interpreted to represent the abandonment of the site after layer (VI).

Our expedition added another phase to the gate's history, floor L12030, found on top of pebble floor L12040. That indicates a more extended period for the gate from what was known before. Our expedition clarified that the gate of Area K had been destroyed only once by fire. Based on our micro-geoarchaeological analysis, this observation opposed the previous suggestions that there were two events of destruction in the gate (Yadin, 1972: 62-63,108-109; Ben-Tor, 1993: 603). The destruction date is not supported by radiometric dates or pottery, as no datable material was found in the excavated area. Here we enter the arena of historical considerations. If the gate's destruction, the city fortification, took place in stratum 1B, the Lower City continued to exist in stratum 1A as an unfortified city. If the destruction had taken place in stratum 1A, the Lower City would have been destroyed in a rather abrupt situation.

6. Conclusions

This research demonstrates an integrative micro-archaeological study for understanding the Bronze Age occupation within the Lower City gate at Tel Hazor. The main agenda was to clarify Yadin's given stratigraphy of human activity and investigate the destruction layer attributed to the end of the Late Bronze Age. The combination of fieldwork and documentation of archaeological material on a macro-level, in combination with micro-archaeological techniques, provides a better understanding of what happened within the gate of Area K. Micro-stratigraphy, preliminary pottery analysis, FTIR spectroscopy, phytolith analysis, and analysis of calcitic micro-remains, supply a combination of proxies to conclude the following:

- Yadin's occupation levels for stratum 3 (MB II-C) and 2 (LB I) were recognized within the stratigraphy of Square K7, yet without evidence for destruction between the strata.
- Indicators of human activities were found in all layers of the profiles of K7 and K5: typical tell site deposits showing variable amounts of anthropogenic materials (e.g., pottery, ash, and phytoliths).

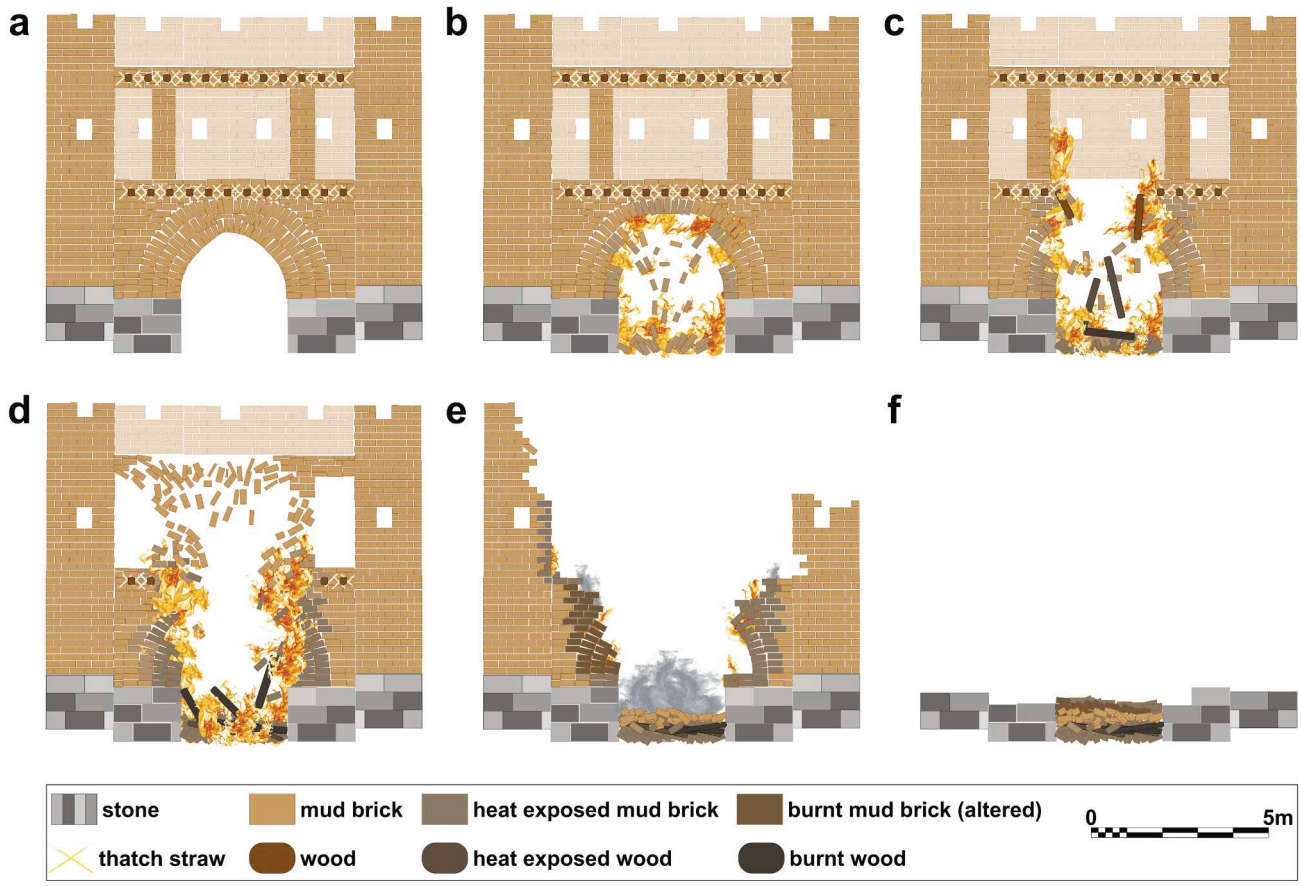

Fig. 14. Reconstruction of the fire in the gate along the western middle pier (after drawing of Tel Dan, Biran1994: 86, Fig. 53). **(a)** Middle pier of the gate. Above transparent, the outer walls of the second floor and the roof terrace are supported by pilasters. Left and right indented the outer casemates or towers. In light yellow thatch, in brown wooden beams supporting the second floor and the terrace. **(b)** Fire event within the gate. **(c)** The collapse of the ceiling and first beams. **(d)** The collapse of pilasters. **(e)** The collapse of the non-burning mud bricks of the second floor and terrace. **(f)** Dark brown layer represents the burnt walls of the passage. Beneath the collapsed unburnt layer of the second floor.

- Sub-strata divisions were made between stratum 3 and stratum 1.
- Macro-archaeological observations suggest to reconsider the sub-divisions suggested in 1989.

The destruction debris in the gate passage is interpreted as one conflagration event (Fig. 14):

The inner part of the roof made of wood beams and thatch was the first to catch fire and collapse, exposing the lower part of the mud bricks walls to elevated temperatures.

The second floor followed and collapsed with an accumulation of a massive construction debris.

Walls left exposed to the elements gradually collapsed and degraded.

Last, our study is the first micro-geoarchaeological study conducted at Hazor. We hope it will encourage more to follow to better understand the history of one of the most important sites in the Levant and further develop an integrated multi-scalar approach to tell sites.

CRediT authorship contribution statement

Marko Runjajić: Conceptualization, Investigation, Writing – original draft, Writing – review & editing, Visualization. **Yosef Garfinkel:** Conceptualization, Writing – original draft, Project administration, Funding acquisition. **Michael G. Hasel:** Project administration, Funding acquisition. **Assaf Yasur-Landau:** Conceptualization, Methodology, Writing – original draft, Project administration, Validation, Funding acquisition, Supervision. **David E. Friesem:** Conceptualization, Methodology, Writing – original draft, Writing – review & editing, Validation, Resources, Funding acquisition, Supervision.

Declaration of Competing Interest

The authors declare that they have no known competing financial interests or personal relationships that could have appeared to influence the work reported in this paper.

Acknowledgement

The 2019 excavations at Area K, Tel Hazor (License G-86/2019) took place in August 2019 for ten excavation days. Y.G., M.G.H., A.Y-L., and Eric H. Cline co-directed the excavation. Ehud Arkin-Shalev acted as the field director, and Katherine Forbes, the register. We thank Igor Kreimerman and Roey Nickelsberg for collecting the sediment samples in the field. We also thank the excavation team and volunteers, including twenty students from the Hebrew University, Southern Adventist University, and the University of Haifa. The Philip and Muriel Berman Center for Biblical Archaeology sponsored the project. A.Y-L. and D.E.F. wish to thank the Computational Research on the Ancient Near East (CRANE), Professors Timothy Harrison and David Schloen for supporting the geoarchaeological research at Hazor and Kabri. M.R. would like to express his gratitude for the Sir Maurice and Lady Irene Hatter Scholarship and the Moriah Rotary Club for their financial support. The sediment analysis took place at the Laboratory of Environmental Micro-History with the support of the University of Haifa startup grant to D.E.

F.. We want to thank Ehud Arkin-Shalev for his help contextualizing the samples, Shira Gur-Arieh for her help with analyzing phytoliths and micro-remains, and Roni Zuckerman-Cooper for her help with processing the samples in the lab. We owe special thanks to Professor Ruth Shahack-Gross and Gal Bermatov-Paz for providing their laboratory facilities. Lastly, M.R. wishes to thank Adellina Cini and Olivia Ayers for their help during the studies.

Appendix A

A summarized overview of the results. Layers referring to discussion 5.1.2.: (I) surface of L12030; (II) collapse of burnt inner structure; (III) collapse of the second floor; (IV) part of the second floor; (V) burnt walls; (VI) post collapse activity; (VII) accumulation/ topsoil. Mineral Compositions: Cl for Clay, a. for altered, n.a. for non-altered, and s.a. for slightly altered; Ca for Calcite and Q for Quartz.

Sample	Sq.	Locus	Layer	Description	color of bulk sample (Munsell values)	Major Mineral Components	phytoliths in M phyt/g sed	wood ash pseudo-morphs in K ash/g sed
1	K5	12033	VII	medium brown	1.1Y 4.4/5.2; 2.1Y 3.4/4.4	Cl (n.a.) > Ca, Q	0.6	
2a	K5	12033	VI	medium brown	9.3YR 4.6/6.3; 9.5YR 3.3/5.9	Cl (n.a.) >> Ca, Q		
2b	K5	12033		red orange		Cl (a.)		
2c	K5	12033		light brown white flake		Cl (a.) >> Q > Ca		
3	K5	12033	VI	light brown with red and white flakes	8.1YR 4/6.6; 7.6YR 3.6/6.3	Ca >>> Cl (n.a.) > Q	1.5	90
4	K5	12033	VI	brown wih red and dark bown flakes	9YR 4.2/6.6; 9.3YR 4.4/6.3	Ca, Cl (n.a.) > Q	0.9	59
5	K5	12033	V-c	light brown with white flakes	1.1Y 5.1/5.7; 1.1Y 4.8/5.6	Ca >> Cl (n.a.) > Q		
6	K5	12033	V-c	light brown	0.7Y 4.8/6.1	Ca >> Cl (s.a.) > Q	0.6	
7	K5	12033	V-c	light brown with white flakes	0.3Y 5.1/6.2; 0.5Y 5.6/6.6	Ca >> Cl (n.a.) > Q		
8	K5	12033	III	light brown with white flakes	0.5Y 5/6.2	Ca, Cl (n.a.) > Q	0.4	235
9	K5	12033	III	light brown	8.9YR 4.6/6.6; 9.9YR 4.9/6	Ca > Cl (n.a.) > Q		
10	K5	12033	II	light brown	8.9YR 4.6/6.6	Ca, Cl(n.a.) > Q	1.2	154
11	K5	12033	II	light brown reddish	7.6YR 2.4/5.5; 6.2YR 3.4/6.8	Cl (n.a.), Ca > Q	1.3	229
12	K5	12033	II-m	medium brown with white and red flakes	1.8Y 2.3/3.8; 9.9YR 2.6/4.9	Cl (a.) > Ca > Q	0.1	
13	K5	12033	II	dark brown	3Y 1.7/2.6	Cl (n.a.) > Q > Ca		59
14	K5	12033	II	dark brown with white and red flakes	1.2Y 2.3/4.3	Cl (n.a.) > Ca, Q		
15	K5	12033	II-m	light brown with white flakes	0.8Y 4.3/5.4; 9.2YR 5/6.4	Ca > Cl (s.a.) >> Q	0.5	241
16	K5	12033	II-m	light brown with white and blackish flakes	1.4Y 4.5/5.6; 1.2Y 5.5/5.8	Cl (n.a.) > Ca > Q	1.1	371
17	K5	12033	II-ap	medium brown with white flakes	2Y 4.2/4.8; 0.5Y 3.9/5.8	Ca, Cl (n.a.) >> Q	1.2	264
18a	K5	12033	II-ap	light brown with white	1.6Y 4.8/5.1; 1.8Y 5.1/5.4	Ca >>> Cl (s.a.)	2.8	401
18b	K5	12033		black flake		Cl (n.a.) >> Q > Ca		
18c	K5	12033		red flake		Cl (a.) >> Q		
18d	K5	12033		white flake		Ca >>> Cl (a.)		
19a	K5	12033	VI	medium brown	8.2YR 3.9/6.8; 9.8YR 5.4/6.9	Cl (n.a.) > Ca > Q		
19b	K5	12033		red orange		Cl (a.) > Q >> Ca		
19c	K5	12033		white flake		Cl (n.a.) >> Ca > Q		
20	K5	12033	V-c	light brown	0.7Y 5.6/6.8; 2.2Y 5.6/5.5	Ca >> Cl (s.a.) > Q	0.5	185
21	K5	12033	III	light to medium reddish brown	0.9Y 4.5/5.7; 8.8YR 3.8/6.2	Cl (n.a.) > Ca > Q		241
22	K5	12033	III	light brown	0.4Y 5.5/6.6; 2Y 4.6/5.5	Cl (n.a.) > Ca > Q	0.8	331
23a	K5	12033	III	light brown	0.6Y 4.5/5.6; 0.4Y 5.1/6.4	Cl (n.a.), Ca > Q	0.9	117
23b	K5	12033		white flake		Ca >>> Cl (a.)		
23c	K5	12033		black material		C		
23c	K5	12033		grey white flake		Ca >>> Cl		
24	K5	12033	II	medium brown	0.8Y 3.2/5.4; 2.1Y 4.1/4.8	Cl (n.a.), Ca > Q		143
25	K5	12033	II-ap	medium brown	2.4Y 3.4/4.6; 9.4YR 3.6/5.5	Cl (n.a.), Ca >> Q	1.3	515
26	K5	12033		medium brown grey with red	8.3YR 3/5.6; 9.5YR 3.9/5.3	Cl (n.a.) > Ca, Q		
27	K5	12033	II-m	dark brown with grey	2.3Y 3.5/3.9; 9.2YR 3.3/5	Ca > Cl (s.a.) > Q		
28a	K5	12033	II-m	mix light dark brown grey	9.7YR 4.7/6.3; 4Y 3.5/3.9	Cl (a.) > Ca, Q	0.2	
28b	K5	12033		dark brown		Cl (a.), Ca > Q		
29	K5	12033	II	dark brown with grey flake	2Y 2.6/3.9; 3.3Y 3/3.9	Ca > Cl (n.a.) >> Q		
30	K5	12033	II-ap	light brown	1Y 5.8/6.1; 2.8Y 6.9/5.8	Ca > Cl (n.a.) >> Q	2.8	511

(*continued on next page*)

(*continued*)

Sample	Sq.	Locus	Layer	Description	color of bulk sample (Munsell values)	Major Mineral Components	phytoliths in M phyt/g sed	wood ash pseudo-morphs in K ash/g sed
31a	K5	12033	II-ap	light brown	2Y 5/4.8; 1.7Y 5.5/5.4	Ca > Cl (n.a.) >> Q	3.9	544
31b	K5	12033		white flake		Ca >>> Cl (n.a.)> Q		
32	K5	12033	II-m	medium greyish brown	4.5Y 3.6/3.8; 4.8Y 4.8/4.1	Ca >>> Cl (a.)		
33a	K5	12033	II-m	medium brown	7.1YR 2.7/6; 8.7YR 3.6/6.1	Cl (a.) > Q >> Ca	0.4	0
33b	K5	12033		reddish brown		Cl (a.) >> Q >> Ca		
33c	K5	12033		grey white		Ca >> Cl (a.) > Q		
34a	K5	12033	II-m	light grey brown		Cl (s.a.) >> Q > Ca		
34b	K5	12033		grey reddish brown		Ca >> Cl (s.a.) > Q		
34c	K5	12033		black brown	0.8Y 2.1/3.7; 4Y 1.8/2.4	Cl (a.) > Q >> Ca		
35a	K5	12033	VI	light brown	8.9YR 4.3/6.4; 8.8YR 3.1/6	Cl (n.a.), Ca >> Q		
35b	K5	12033		red orange		Cl (a.) >> Q >> Ca		
35c	K5	12033		white flake		Ca >> Cl (a.) > Q		
36	K5	12033	V; V-c	light brown	0.7Y 5.8/6.4; 9.9YR 5.4/6.4	Ca >>> Cl (a.)	1.9	
37a	K5	12033	V-c	light brown	9.9YR 5.1/6; 8.8YR 5.2/7.1	Ca >> Cl (n.a.) >> Q		
37b	K5	12033		white flake		Ca >>> Cl (a.)		
38	K5	12033	IV; V-c	light brown	1.7Y 5.2/5.5	Ca >> Cl (n.a.) > Q		
39	K5	12033	IV; V-c	light brown	0.2Y 5.1/6	Ca >> Cl (a.) > Q		
40a	K5	12033	III; V-c	light brown	9.3YR 4.8/6.3	Ca > Cl (n.a.) >> Q	0.5	286
40b	K5	12033		white flake		Ca >>> Cl (a.)		
41a	K5	12033	IV; V-c	light brown	9.5YR 5.8/6.8	Ca, Cl (n.a.) >> Q		229
41b	K5	12033		white flake with light brown		Ca >>> Cl (s.a.) , Q		
41c	K5	12033		light brown		Ca > Cl (n.a.) >> Q		
42a	K5	12033	III	medium brown	9.7YR 5.1/5.4; 9.4YR 4.3/5.7	Ca > Cl (n.a.) > Q	0.8	59
42b	K5	12033		orange flake		Cl (a.) >> Q >> Ca		
43a	K5	12033	III	light grey brown	9.4YR 4.4/5.9; 2.1Y 4/4.3	Ca >= Cl (n.a.) > Q		93
43b	K5	12033		white flake		Ca >>> Cl (a.)		
44a	K5	12033	III	medium grey brown	1.3Y 3.8/4.7; 2.1Y 4/4.3	Cl (n.a.), Ca >> Q		0
44b	K5	12033		white flake		Ca >>> Cl (n.a.)		
45a	K5	12033	II-ap	medium brown with white and orange	1.1Y 3.4/4.3	Ca > Cl (n.a.) >> Q	1.3	286
45b	K5	12033		white flake		Ca > Cl (n.a.) >> Q		
46a	K5	12033	II-ap	light grey brown	1.5Y 4.6/5	Ca, Cl (n.a.) >> Q	2.0	176
46b	K5	12033		white flake		Ca >>> Cl (n.a.) > Q		
47	K5	12033	II-p	light grey brown	0.5Y 5.5/5.8	Ca > Cl (n.a.) >> Q	3.4	200
48a	K5	12033	II-ap	light grey brown	9.9YR 5/6.1	Ca > Cl (n.a.) >> Q	1.7	251
48b	K5	12033		white flake		Ca >>> Cl (a.) > Q		
49	K5	12033	V	light brown	8.9YR 4.4/6.2	Ca > Cl (s.a.) > Q		
50a	K5	12033	IV	light brown	8.7YR 4.5/6.1	Cl (n.a.), Ca >> Q		
50b	K5	12033		white flake		Ca >>> Cl (n.a.), Q		
51a	K5	12033	III	light brown	1.9Y 5.8/5.6; 9.7YR 4.4/5.7	Ca >> Cl (n.a.) >> Q		
51b	K5	12033		white flake		Ca >>> Cl (s.a.) > Q		
52a	K5	12034	III	medium brown	10YR 3.9/4.9	Ca > Cl (n.a.) >> Q	1.3	278
52b	K5	12034		white flake		Ca >>> Cl (s.a.)		
53a	K5	12034	III	light brown	1.5Y 5/4.9	Ca, Cl (n.a.) >> Q	2.5	150
53b	K5	12034		white flake		Ca >>> Cl (s.a.) > Q		
54a	K5	12034	II-p	light brown	1.2Y 6/5.7	Ca > Cl (n.a.) >> Q	3.5	200
54b	K5	12034		white flake		Ca >>> Cl (n.a.) > Q		
55a	K5	12034	II-pl	light brown	9.9YR 5.2/5.8	Ca > Cl (n.a.) >> Q	2.5	323
55b	K5	12034		white flake		Ca >>> Cl (s.a.) > Q		
56a	K5	12034	IV	medium brown	9.3YR 3.6/5.9	Ca >= Cl (n.a.) >> Q	1.4	335
56b	K5	12034		white flake		Ca >> Cl (a.) > Q		
57a	K5	12034	IV	brown	4.7YR 4.2/6.6; 5Y 2.3/2.8	Ca, Cl (n.a.) >> Q		
57b	K5	12034		brown black		Cl (a.) > Q > Ca		
57c	K5	12034		reddish		Cl (a.) >> Q >> Ca		
58a	K5	12034	III	medium brown	0.9Y 3.4/4.9	Cl (n.a), Ca >> Q		
58b	K5	12034		white flake		Ca >>> Cl (a.), Q		
59a	K5	12034	II-p	light brown	1.8Y 5.9/5.3; 1.1Y 3.9/5	Ca > Cl (n.a.) >> Q	3.4	143
59b	K5	12034		white flake		Ca >>> Cl (s.a.)		
60	K5	12034	II-pl	light brown	1.1Y 4.7/5.4; 0.3Y 4.4/5.1	Ca >> Cl (n.a.) > Q	1.4	120
61a	K5	12034	VI	medium brown	9.3YR 3.2/6; 6YR 2.8/6.6	Ca, Cl (n.a.) >> Q	1.1	
61b	K5	12034		white flake		Ca >>> Cl (a.) > Q		
62	K5	12034	IV	medium brown	1.7Y 3.3/4.2; 9.9YR 4.3/6	Cl (n.a.), Ca >> Q		
63a	K5	12034	III	medium brown	1.2Y 3.7/4.5	Cl (n.a.) >> Ca > Q	1.9	112
63b	K5	12034		white flake		Ca >>> Cl (s.a.)		
63bn	K5	12034		white flake		Ca >>> Cl (n.a.) > Q		
64a	K5	12034	II-p	light brown	2.6Y 5.8/5.3; 1.9Y 5/5.3	Ca > Cl (n.a.) >> Q	3.8	176
64b	K5	12034		white flake		Ca >>> Cl (n.a.) > Q		

(*continued on next page*)

(*continued*)

Sample	Sq.	Locus	Layer	Description	color of bulk sample (Munsell values)	Major Mineral Components	phytoliths in M phyt/g sed	wood ash pseudo-morphs in K ash/g sed
65a	K5	12034	II-a	light brown	3.2Y 5.5/5.3; 1.6Y 5.9/5.7	Ca, Cl (n.a.) >> Q	2.0	421
65b	K5	12034		white flake		Ca >>> Cl (s.a.) > Q		
65c	K5	12034		black flake with white		Ca >>> Cl (s.a.) > Q		
66a	K5	12034	IV	medium brown with white	9.6YR 3.3/5.9; 9.2YR 4/5.8	Cl (n.a.) > Ca >> Q		
66b	K5	12034		white flake		Ca >>> Cl (n.a.) > Q		
66c	K5	12034		red flake		Cl (a.) >> Q > Ca		
67a	K5	12034	III	medium brown	2Y 5.4/5.5; 5.9Y 7.7/4.4	Cl (n.a.) > Ca > Q	2.5	271
67b	K5	12034		light grey brown		Ca > Cl (n.a.) >> Q		
67c	K5	12034		white flake		Ca >>> Cl (a.), Q		
68a	K5	12034	II-p; II-a	light brown	2.3Y 5.9/5.1; 1.4Y 5.3/5.6	Ca >>> Cl (a.) > Q	3.9	440
68b	K5	12034		white flake		Ca >>> Cl (a.), Q		
69a	K5	12034	II-pl	light brown	1.2Y 4.4/5.3; 1.8Y 4/4.7	Cl (n.a.), Ca >> Q	1.9	84
69b	K5	12034		white flake		Ca >>> Cl (n.a.) > Q		
70a	K5	12034	III	light brown	1.7Y 5.1/5.6; 1.8Y 6/5.5	Ca > Cl (n.a.) >> Q	2.2	150
70b	K5	12034		white flake		Ca >>> Cl (a.) > Q		
71a	K5	12034	II-pl	light brown	2.5Y 4.8/5; 0.7Y 4.5/5.2	Cl (n.a.) > Ca >> Q	2.2	323
71b	K5	12034		light brown white		Ca >> Cl (n.a.) >> Q		
72a	K5	12034	III	light brown with white	0.6Y 5/6.3; 1.8Y 6.1/5.8	Ca > Cl (n.a.) >> Q	1.8	124
72b	K5	12034		white flake		Ca >>> Cl (a.) > Q		
73a	K5	12030	I	light grey brown	0.7Y 4.3/4.8	Cl (n.a.), Ca >> Q	3.7	343
73b	K5	12030		light grey		Ca > Cl (n.a.) >> Q		
74a	K5	12030	I	light brown	3.4Y 5.8/4.9; 1.7Y 5.4/5.4	Ca > Cl (n.a.) >> Q	3.5	59
74b	K5	12030		white flake		Ca >>> Cl (a.)		
75a	K7	12014		light brown with medium brown	9.4YR 3.1/5.4; 0.7Y 3.4/5.1	Cl (n.a.) > Ca > Q	0.9	0
75b	K7	12014		dark		Cl (n.a.) > Ca > Q		
76a	K7	12014		light brown	2.5Y 5.3/5	Ca, Cl (n.a.) >> Q	3.6	168
76b	K7	12014		white flake		Cl (a.) >>> Ca > Q		
77a	K7	12040		medium brown	9.5YR 3.9/5.3	Cl (n.a.) > Ca > Q	1.4	59
77b	K7	12040		medium light brown		Ca, Cl (n.a.) >> Q		
77c	K7	12040		red flake		Cl (a.) >> Q > Ca		
78a	K7			medium brown with black and white flakes		Cl (n.a.) > Ca > Q	1.2	88
78b	K7			dark medium brown	1Y 3.6/4.5	Cl (a.) >> Q > Ca		
79	K7	12045		yellowish white	4.5Y 7.1/5; 9.4YR 4/5.4	Ca >>> Cl (s.a.)	0.0	59
80	K7	12016		light medium brown	1.1Y 5.1/5.3; 9.4YR 4/5.4	Ca, Cl (n.a.) > Q	1.3	331
81	K7	12016		medium dark brown	2.9Y 3.6/3.9; 3Y 4.1/4.1	Cl (n.a.), Ca >> Q	2.3	117
82a	K7	12016		light brown	2Y 5.5/5.4; 1.1Y 5/5.9	Ca, Cl (n.a.) >> Q	2.0	172
82b	K7	12016		white flake		Ca >>> Cl (s.a.)		
82c	K7	12016		red flake coloured		Q, Cl (n.a.) > Ca		
83a	K7	12016		medium brown	2.4Y 4.8/4.9; 5.3Y 4.5/3.3	Cl (n.a.), Ca >> Q	4.8	241
83b	K7	12016		white material		Ca >>> Cl (n.a.)		
84a	K7	12016		light brown grey	2Y 4.4/4.9; 1.3Y 4.1/4.7	Cl (n.a.), Ca >> Q	0.9	271
84b	K7	12016		white flake		Ca >>> Cl (n.a.) > Q		
85a	K7	12060		yellowish white bown	4.2Y 6.6/6.5	Ca >> Cl (n.a.) > Q	0.4	147
85b	K7	12060		yellowish white		Ca >>> Cl (n.a.)		
85c	K7	12060		light brown reddish		Cl (n.a.) >> Ca, Q		
85d	K7	12060		medium brown flake		Cl (s.a.) >> Ca, Q		
86a	K7	12062		light brown grey	0.3Y 4.5/4.4; 1.7Y 5.5/5.4	Ca > Cl (n.a.) > Q	1.5	86
86b	K7	12062		white yellow flake		Ca >>> Cl (n.a.) > Q		
86c	K7	12062		red brown flake		Cl (a.), Q >>> Ca		
87a	K7	12065		white yellowish	4.7Y 7.2/5.4; 5.2Y 7.5/3.8	Ca >>> Cl (n.a.), Q		150
87b	K7	12065		light brown reddish		Cl (n.a.) >= Ca > Q		
87c	K7	12065		black flake		Cl (a.) > Q >> Ca		
88a	K7	12067		medium brown	9.5YR 3.9/5.3	Ca, Cl (n.a.) >> Q	1.1	205
88b	K7	12067		white flake		Ca >>> Cl (n.a.), Q		
88c	K7	12067		black flake		Cl (n.a.) >> Q >> Ca		
89a	K7	12016		light grey brown	0.8Y 4.2/5.7;	Ca, Cl (n.a.) >> Q	0.8	401
89b	K7	12016		white flake		Ca >>> Cl (n.a.) > Q		
89c	K7	12016		dark brown		Cl (n.a.) >> Q >> Ca		
90a	K7	12060		yellowish white	4.6Y 6.6/5.9	Ca >>> Cl (n.a.) > Q	0.4	
90b	K7	12060		light brown		Ca >> Cl (n.a.) >> Q		

References

Albert, R.M., Shahack-Gross, R., Cabanes, D., Gilboa, A., Lev-Yadun, S., Portillo, M., Sharon, I., Boaretto, E., Weiner, S., 2008. Phytolith-rich layers from the Late Bronze and Iron Ages at Tel Dor (Israel): mode of formation and archaeological significance. J. Archaeol. Sci. 35 (1), 57–75. https://doi.org/10.1016/j.jas.2007.02.015.

Arkin-Shalev, E., Garfinkel, Y., Cline, E.H., Hasel, M., Yasur-Landau, A., 2019. Excavation file: Hazor Area K G-86 2019, 106.

Bechar, S., Ben-Tor, A., Wachtel, I., Ben-Tor, D., Boaretto, E., Stockhammer, P.W., 2021. The Destruction of Late Bronze Age Hazor. Ägypten und Levante 31, 45–74. https://doi.org/10.1553/AEundL31s45.

Ben-Tor, A., 2016. Hazor: Canaanite Metropolis, Israelite City. Israel Exploration Society and Biblical Archaeology Society, Jerusalem.

Ben-Tor, A., 1993. The New encyclopedia of archaeological excavations in the Holy Land. In: Stern, E., Lewinson-Gilboa, A., Aviram J. (Eds.), The New encyclopedia of archaeological excavations in the Holy Land 2, pp. 594–606.

Ben-Tor, A., Bonfil, R., Paris, A., 1997. Hazor V : an account of the fifth season of excavation, 1968: text and illustrations. Israel Exploration Society, Jerusalem.

Ben-Tor, A., Zuckerman, S., 2008. Hazor at the End of the Late Bronze Age: Back to Basics. Bull. Am. Sch. Orient. Res. 350, 1–6. https://doi.org/10.1086/BASOR25609263.

Ben-Tor, A., ed., Yadin, Y., Aharoni, Y, Amiran, R., Dothan, M., Dothan, T., Dunayevski, I., Geva, S., Stern, E., 1989. Hazor III–IV: An Account of the Third and Fourth Seasons of Excavation, 1957–1958. Text. Israel Exploration Society, Jerusalem.

Ben-Tor, A., Zuckerman, S., Bechar, S., Sandhaus, D., Kuper-Blau, T., Avrutis, V.W., 2017. Hazor VII: the 1990-2012 excavations, the Bronze Age. *Israel Exploration Society*; Institute of Archaeology, Hebrew University of Jerusalem, Jerusalem.

Berna, F., Behar, A., Shahack-Gross, R., Berg, J., Boaretto, E., Gilboa, A., Sharon, I., Shalev, S., Shilstein, S., Yahalom-Mack, N., Zorn, J.R., Weiner, S., 2007. Sediments exposed to high temperatures: reconstructing pyrotechnological processes in Late Bronze and Iron Age Strata at Tel Dor (Israel). J. Archaeol. Sci. 34 (3), 358–373. https://doi.org/10.1016/j.jas.2006.05.011.

Biran, A., 1994. Biblical Dan. Israel Exploration Society: Jerusalem.

Burke, A.A., 2008. "Walled up to Heaven": The Evolution of Middle Bronze Age Fortification Strategies in the Levant. Winona Lake: Eisenbrauns.

Canti, M.G., 1997. An investigation of microscopic calcareous spherulites from herbivore dungs. J. Archaeol. Sci. 24 (3), 219–231. https://doi.org/10.1006/jasc.1996.0105.

Canti, M.G., Brochier, J.É., 2017. Faecal Spherulites. Archaeological Soil and Sediment Micromorphology, Canti 1998, 51–54. https://doi.org/10.1002/9781118941065.ch5.

Chu, V., Regev, L., Weiner, S., Boaretto, E., 2008. Differentiating between anthropogenic calcite in plaster, ash and natural calcite using infrared spectroscopy: implications in archaeology. J. Archaeol. Sci. 35 (4), 905–911. https://doi.org/10.1016/j.jas.2007.06.024.

Cline, E.H., 2014. 1177 B.C.: The Year Civilization Collapsed. Princeton University Press, Princeton.

Eliyahu-Behar, A., Shilstein, S., Raban-Gerstel, N., Goren, Y., Gilboa, A., Sharon, I., Weiner, S., 2008. An integrated approach to reconstructing primary activities from pit deposits: iron smithing and other activities at tel dor under neo-assyrian domination. J. Archaeol. Sci. 35 (11), 2895–2908. https://doi.org/10.1016/j.jas.2008.06.004.

Finkelstein, I. 2005. Hazor at the End of the Late Bronze Age: A Reassessment. In Dietrich M., and Loretz O., eds. Ugarit-Forschungen Internationales Jahrbuch für die Altertumskunde Syrien-Palästinas 37, 341–349. Münster.

Forget, M.C.L., Regev, L., Friesem, D.E., Shahack-Gross, R., 2015. Physical and mineralogical properties of experimentally heated chaff-tempered mud bricks: Implications for reconstruction of environmental factors influencing the appearance of mud bricks in archaeological conflagration events. J. Archaeol. Sci. Rep. 2, 80–93. https://doi.org/10.1016/j.jasrep.2015.01.008.

Friesem, D., Boaretto, E., Eliyahu-Behar, A., Shahack-Gross, R., 2011. Degradation of mud brick houses in an arid environment: a geoarchaeological model. J. Archaeol. Sci. 38 (5), 1135–1147. https://doi.org/10.1016/j.jas.2010.12.011.

Friesem, D.E., Tsartsidou, G., Karkanas, P., Shahack-Gross, R., 2014. Where are the roofs? A geo-ethnoarchaeological study of mud brick structures and their collapse processes, focusing on the identification of roofs. Archaeol. Anthropol. Sci. 6 (1), 73–92. https://doi.org/10.1007/s12520-013-0146-3.

Friesem, D.E., Anton, M., Waiman-Barak, P., Shahack-Gross, R., Nadel, D., 2020. Variability and complexity in calcite-based plaster production: A case study from a Pre-Pottery Neolithic B infant burial at Tel Ro'im West and its implications to mortuary practices in the Southern Levant. J. Archaeol. Sci. 113, 105048 https://doi.org/10.1016/j.jas.2019.105048.

Goshen, N., Yasur-Landau, A., Cline, E.H., Shahack-Gross, R., 2017. Palatial architecture under the microscope: Production, maintenance, and spatiotemporal changes gleaned from plastered surfaces at a Canaanite palace complex, Tel Kabri, Israel. J. Archaeol. Sci. Rep. 11, 189–199. https://doi.org/10.1016/j.jasrep.2016.11.039.

Gur-Arieh, S., Mintz, E., Boaretto, E., Shahack-Gross, R., 2013. An ethnoarchaeological study of cooking installations in rural Uzbekistan: Development of a new method for identification of fuel sources. J. Archaeol. Sci. 40 (12), 4331–4347. https://doi.org/10.1016/j.jas.2013.06.001.

Gur-Arieh S., Shahack-Gross R., 2020. Ash and Dung Calcitic Micro-remains. In: Henry A., eds. Handbook for the Analysis of Micro-Particles in Archaeological Samples. Interdisciplinary Contributions to Archaeology. Springer, Cham. 117–147.

Gur-Arieh, S., Shahack-Gross, R., Maeir, A.M., Lehmann, G., Hitchcock, L.A., Boaretto, E., 2014. The taphonomy and preservation of wood and dung ashes found in archaeological cooking installations: case studies from Iron Age Israel. J. Archaeol. Sci. 46 (46), 50–67. https://doi.org/10.1016/j.jas.2014.03.011.

Katz, O., Cabanes, D., Weiner, S., Maeir, A.M., Boaretto, E., Shahack-Gross, R., 2010. Rapid phytolith extraction for analysis of phytolith concentrations and assemblages during an excavation: An application at Tell es-Safi/Gath. Israel. *Journal of Archaeological Science* 37 (7), 1557–1563. https://doi.org/10.1016/j.jas.2010.01.016.

Knapp, A.B., Manning, S.W., 2016. Crisis in Context: The End of the Late Bronze Age in the Eastern Mediterranean. Am. J. Archaeol. 120 (1), 99–149. https://doi.org/10.3764/aja.120.1.0099.

Kreimerman, I., 2017. A Typology for Destruction Layers. The Late Bronze Age Southern Levant as a Case Study. In T. Cunningham and J. Driessen, eds. Crisis to Collapse: The Archaeology of Social Breakdown, Aegis 11, 173-203. Presses Universitaires de Louvain: Louvain-la-Neuve.

Kreimerman, I., 2021. After the Flames Died Down: Defeat, Destruction and Forced Abandonment in the Bronze and Iron Age Levant. In: Culture of Defeat: Submission in Written Sources and the Archaeological Record. Proceedings of a Joint Seminar of the Hebrew University of Jerusalem and the University of Vienna, October 2017, edited by K. Streit and M. Grohmann, Piscataway, NJ, USA: Gorgias Press, 229-260. 10.31826/9781463241889-012.

Kreimerman, I., Shahack-Gross, R., 2019. Understanding conflagration of one-story mud-brick structures: an experimental approach. Archaeol. Anthropol. Sci. 11, 2911–2928. https://doi.org/10.1007/s12520-018-0714-7.

Namdar, D., Zukerman, A., Maeir, A.M., Katz, J.C., Cabanes, D., Trueman, C., Shahack-Gross, R., Weiner, S., 2011. The 9th century BCE destruction layer at Tell es-Safi/Gath, Israel: Integrating macro- and microarchaeology. J. Archaeol. Sci. 38 (12), 3471–3482. https://doi.org/10.1016/j.jas.2011.08.009.

Piperno, D.R., 2006. Phytoliths: a comprehensive guide for archaeologists and paleoecologists. Rowman AltamiraPress, Oxford.

Poduska, K.M., Regev, L., Boaretto, E., Addadi, L., Weiner, S., Kronik, L., Curtarolo, S., 2011. Decoupling Local Disorder and Optical Effects in Infrared Spectra: Differentiating Between Calcites with Different Origins. Adv. Mater. (Weinheim) 23 (4), 550–554. https://doi.org/10.1002/adma.201003890.

Regev, L., Poduska, K.M., Addadi, L., Weiner, S., Boaretto, E., 2010. Distinguishing between calcites formed by different mechanisms using infrared spectrometry: Archaeological applications. J. Archaeol. Sci. 37 (12), 3022–3029. https://doi.org/10.1016/j.jas.2010.06.027.

Regev, L., Cabanes, D., Homsher, R., Kleiman, A., Weiner, S., Finkelstein, I., Shahack-Gross, R., 2015. Geoarchaeological Investigation in a Domestic Iron Age Quarter, Tel Megiddo, Israel. Bull. Am. Sch. Orient. Res. 374, 135–157. https://doi.org/10.5615/bullamerschoorie.374.0135.

Sapir, Y., Avraham, A., Faust, A., 2016. Mud-brick composition, archeological phasing and pre-planning in Iron Age structures: Tel 'Eton (Israel) as a test-case. Archaeol. Anthropol. Sci. 10 (2), 337–350. https://doi.org/10.1007/s12520-016-0350-z.

Shahack-Gross, R., Albert, R.M., Gilboa, A., Nagar-Hilman, O., Sharon, I., Weiner, S., 2005. Geoarchaeology in an urban context: The uses of space in a Phoenician monumental building at Tel Dor (Israel). J. Archaeol. Sci. 32 (9), 1417–1431. https://doi.org/10.1016/j.jas.2005.04.001.

Shahack-Gross, R., Gafri, M., Finkelstein, I., 2009. Identifying Threshing Floors in the Archaeological Record: A Test Case at Iron Age Tel Megiddo, Israel. J. Field Archaeol. 34 (2), 171–184. https://doi.org/10.1179/009346909791070943.

Shahack-Gross, R., 2011. Herbivorous livestock dung: Formation, taphonomy, methods for identification, and archaeological significance. J. Archaeol. Sci. 38 (2), 205–218. https://doi.org/10.1016/j.jas.2010.09.019.

Singer, A., 2007. The Soils of Israel. Berlin: Springer-Verlag. 10.1007/978-3-540-71734-8.

Stager, L.E., Schloen, J.D., Voss, R.J., Aja, A.J., 2018. Ashkelon 6: The Middle Bronze Age ramparts and gates of the north slope and later fortifications. Eisenbrauns, University Park, Pennsylvania.

Tsartsidou, G., Lev-Yadun, S., Albert, R.M., Miller-Rosen, A., Efstratiou, N., Weiner, S., 2007. The phytolith archaeological record: strengths and weaknesses evaluated based on a quantitative modern reference collection from Greece. J. Archaeol. Sci. 34 (8), 1262–1275. https://doi.org/10.1016/j.jas.2006.10.017.

Weiner, S., 2010. Microarchaeology: beyond the visible archaeological record. New York: Cambridge University Press.

Yadin, Y., 1959. The Fourth Season of Excavations at Hazor. Biblic. Archaeol. 22, 1–20. https://doi.org/10.2307/3209103.

Yadin, Y., 1969. The Fifth Season of Excavations at Hazor, 1968–1969. Biblic. Archaeol. 32, 50–71. https://doi.org/10.2307/3211006.

Yadin, Y., 1972. Hazor: The Schweich Lectures of the British Academy, 1970. Oxford University Press. London.

Yadin, Y., Aharoni, Y., Dunayevski, T., Dothan, R., 1961. Perrot, eds. Hazor III-IV: An Account of the Third and Fourth Seasons of Excavations, 1957-1958: Plates. Jerusalem: Israel Exploration Society.

Zuckerman, S., 2007. Anatomy of a destruction: Crisis architecture, termination rituals and the fall of Canaanite Hazor. JMA 20, 3–32. 10.1558/jmea.2007.v20i1.3.

Zuckerman, S., 2011. Ruin cults at Iron I Hazor, in The Fire Signals of Lachish: Studies in the Archaeology and History of Israel in the Late Bronze Age, Iron Age, and Persian Period in Honor of David Ussishkin, edited by I. Finkelstein and N. Na'aman, Winona Lake. Eisenbraus. 387-394.

Zuckerman, S., 2012. In: Kamla, J. (Ed.), The temples of Canaanite Hazor. In: *Temple Building and Temple Cult*. Harrasowitz, Wiesbaden, pp. 99–125.